

Complex Analysis of Askaryan Radiation: A Fully Analytic Model in the Time-Domain

Jordan C. Hanson* and Raymond Hartig
Department of Physics and Astronomy, Whittier College
(Dated: April 28, 2022)

The detection of ultra-high energy (UHE, >10 PeV) neutrinos via detectors designed to utilize the Askaryan effect has been a long-time goal of the astroparticle physics community. The Askaryan effect describes radio-frequency (RF) radiation from high-energy cascades. When a UHE neutrino initiates a cascade, cascade properties are imprinted on the radiation. Thus, observed radiation properties must be used to reconstruct the UHE neutrino event. Analytic Askaryan models have three advantages when used for UHE neutrino reconstruction. First, when analytic models are matched to observed data, cascade properties may be calculated directly from single RF waveforms. Second, fully analytic models require no Monte Carlo simulation of cascade particle trajectories, minimizing computational intensity. Third, fully analytic models can be embedded in firmware to enhance the real-time sensitivity of detectors. We derive a fully analytic Askaryan model in the time-domain given the energy and geometry of the UHE neutrino-induced cascade. We compare the fully analytic model to a semi-analytic parameterization used commonly in NuRadioMC, a simulation being used to design IceCube-Gen2. We find correlation coefficients greater than 0.95 between the fully analytic and semi-analytic cases, and we find the total power in the signals agree to within 5%.

I. INTRODUCTION

The flux of neutrinos originating from outside the solar system with energies between [0.01-1] PeV has been measured by the IceCube collaboration [1]. Previous analyses have shown that the discovery of UHE neutrinos (UHE- ν) will require an upgraded detector design with a larger effective volume because the flux is expected to decrease with energy [2–6]. Neutrinos with energies above 10 PeV could potentially explain the origin of UHE cosmic rays (UHECR), and provide the chance to study electroweak interactions at record-breaking energies [7, 8]. Utilizing the Askaryan effect greatly expands the effective volume of UHE- ν detector designs, because this effect offers a way to detect UHE- ν with radio pulses that travel more than 1 kilometer in sufficiently RF-transparent media such as Antarctic and Greenlandic ice [9–11].

The Askaryan effect occurs within a dense medium of refractive index n when a relativistic particle with $v > c/n$ initiates a high-energy cascade with negative total charge. The charge radiates in the RF bandwidth, and the radiation may be detected by RF channels if the medium is RF-transparent [12] [13]. If the primary particle initiating the cascade is a UHE- ν , the medium must have both sufficient RF transparency and sufficient volume to capture the signals. Analyses from the recent ANITA-IV flight placed upper limits on the differential flux, assuming a pure E_ν^{-2} spectrum from $E_\nu \in [10^{18}, 10^{21}]$ eV of $E_\nu^2 \phi_\nu \leq 2.2 \times 10^{-7}$ GeV cm $^{-2}$ s $^{-1}$ sr $^{-1}$ [14]. Accounting for the flux, arrays of $\mathcal{O}(100)$ *in situ* detectors that encompass effective areas of $\approx 10^4$ m 2 sr per station build discovery sensitivity when spaced by approximately one RF attenuation length. Because such

ice formations with sufficient volume are abundant in Antarctica and Greenland, there is now a well-developed field of prototype Askaryan-class detectors in Antarctica and Greenland that seek Askaryan radiation from UHE- ν . Increasingly strict upper limits have been placed on the UHE- ν flux from astrophysical and cosmogenic sources [5, 6, 14, 15]. The IceCube Collaboration has also published upper limits on UHE- ν flux, and that work indicated that a large in-ice detector would be necessary to reach the desired sensitivity [4].

Askaryan radiation was first measured in the laboratory in silica sand, and later ice [16–18]. The effects that govern the amplitude and phase of the radiation are understood. At RF wavelengths, individual cascade particles radiate coherently, and the overall amplitude scales with the total track length of the excess negative charge. The *longitudinal length* along the cascade axis determines the RF pulse shape, and the radiation must be observed near the Cherenkov angle. The *excess charge profile* of a cascade is a function that describes the excess negative charge versus position along the cascade axis. The radiation proceeds from the region near the cascade maximum, which may be approximated by a Gaussian function. At energies far above 10 PeV, however, the charge excess profile can have many local maxima due to the LPM effect [19, 20]. Wavelengths that are shorter than the *lateral width* of the cascade, perpendicular to the cascade axis, are attenuated. The lateral cascade width has the effect of a low-pass filter on the radiation [20]. Thus, a theoretical foundation has been constructed from a variety of experimental results.

The field of Askaryan-class detectors requires this foundation for at least two reasons. First, the theoretical form of the Askaryan electromagnetic (EM) field is used to optimize RF detector designs. Askaryan models are incorporated into simulations [21–23] in order to calculate the expected signal in a real detector. Recent

*Electronic address: jhanson2@whittier.edu

Askaryan reconstruction tools for the radio component of IceCube-Gen2 combine machine learning and insights from Askaryan radiation physics [24–26]. Second, theoretical models may be used as templates to search large data sets for signal candidates when combined with RF impulse response [5, 27]. At the UHE-scale, the EM field-strengths of kiloVolts per meter are expected a few meters from the cascade. However, the detected signal-to-noise ratios (SNRs) at RF channels are expected to be small ($\text{SNR} \approx 2$) because the typical vertex separation is ≈ 1 km. The amplitude of the EM field decreases with the distance to the vertex ($1/r$), and there is some alteration of the signal by the ice [9, 28, 29]. The combination of low SNR and RF sampling frequency for the signal bandwidth of [0.1-1] GHz implies that RF channels are triggered at high rate by RF thermal noise. The thermal trigger rate causes potential UHE- ν signals to be hidden within millions of thermal trigger waveforms. Thus, template waveform analysis and other digital signal processing approaches must be used to isolate rare signals.

Askaryan models fall into three categories: full MC, semi-analytic, and fully analytic. The original work by E. Zas, F. Halzen, and T. Stanev (ZHS) [13] was a full MC model. The basic properties of the EM radiation from cascades up to 1 PeV were reproduced with threshold energies of 0.5-1 MeV. Sub-threshold particles were assumed to lose energy to processes like the photo-electric effect and not contribute to the EM radiation. Overall signal amplitude was found to scale with energy because energy scales with the total weighted, projected track length. A parameterization for the EM field below 1 GHz was offered, attenuating modes above 1 GHz via a frequency-dependent form factor. The form factor cutoff frequency may be related to the lateral cascade width [20]. The semi-analytic approach was introduced by J. Alvarez-Muñiz *et al* (ARVZ) to account for the non-Gaussian fluctuations in the charge excess profile caused by the LPM effect, while keeping the form factor analytic when the EM radiation is observed at the Cherenkov angle [19]. The final EM wave is obtained from the negative derivative of the vector potential once it has been convolved with the charge excess profile, accounting for the viewing angle. The vector potential at the Cherenkov angle is labeled the form factor. Recent work also accounts for differences in fit parameters from simulated EM and hadronic cascades, and other interaction channels, while matching full MC field amplitudes to within a few percent [30].

Finally, analytic models that reproduce the features of Askaryan radiation from first principles have been introduced. J. Ralston and R. Buniy (RB) introduced a fully analytic model valid for cascades with longitudinal length greater than or less than the length over which EM radiation is coherent, encapsulated by a parameter η [31]. The goal was to create a model valid in the near and far-fields of the EM radiation. Recently, a model was introduced by J. C. Hanson and A. Connolly (JCH+AC) that built upon RB by providing an analytic form factor

derived from GEANT4 simulations, and accounted for LPM elongation of the longitudinal cascade width [20]. The form factor and the RB coherence effect formed a set of poles in the complex plane that filter the EM radiation in the same way a multi-pole low-pass filter governs analog signals. The LPM treatment in JCH+AC increased the longitudinal length at energies far above the LPM energy (0.3 PeV in ice), but did not account for the deviation from Gaussian behavior caused by sub-showers in the LPM effect. Both RB and JCH+AC expressed the model generally in the Fourier domain. However, an example EM field was provided in the time-domain if the field is observed at the Cherenkov angle. *The theme of this work is to present a fully analytic time-domain model valid for all viewing angles, provided that $\eta < 1$.*

In Section II, the cascade geometry, units, and relevant vocabulary are defined. In Section III, we present the derivation of the form factor from first principles. Appendix A of the JCH+AC publication contains the detailed comparison between GEANT4 cascade simulations and theoretical predictions for the lateral charge distribution. In Section IV, a new derivation of the Askaryan EM field observed at the Cherenkov angle (*on-cone*) is presented that accounts for the relative strength of one complex pole from coherence effects and two from the form factor. In Section V, a new derivation of the Askaryan EM field not observed at the Cherenkov angle (*off-cone*) is presented that accounts for the longitudinal cascade width, viewing angle, and form factor. In Section VI, analytical results are compared to published Askaryan EM fields generated by NuRadioMC [23] at 10 PeV and 100 PeV. At this energy, the LPM effect only has a small influence on the cascade development. In Section VII, the results are summarized and several applications of the new analytic model are described.

II. UNITS, DEFINITIONS, AND CONVENTIONS

The coordinate system of the Askaryan radiation from a vector current density \vec{J} is shown in Figure 1 (a)-(b). Primed coordinates refer to the cylindrical coordinate system of the high-energy cascade. The zenith or *viewing angle* is measured with respect to the *longitudinal axis* (z'). The separation between the origin and observer is $r = |\vec{x} - \vec{x}'|$, in the \hat{r} direction in spherical observer coordinates. The origin is located along the longitudinal axis where the cascade has the highest instantaneous charge density (ICD). The cascade is assumed to generate an ICD with cylindrical symmetry and therefore no dependence on ϕ' . This assumption is based on the large number of cascade particles, and the conservation of momentum. The lateral extent of the ICD is along the *lateral axis* (ρ'). The viewing angle in Figure 1 (a)-(b) is θ in spherical coordinates, and the Cherenkov angle occurs when θ satisfies $\cos(\theta_C) = 1/n_{\text{ice}}$. The index value for solid ice is $n_{\text{ice}} = 1.78 \pm 0.003$ [32].

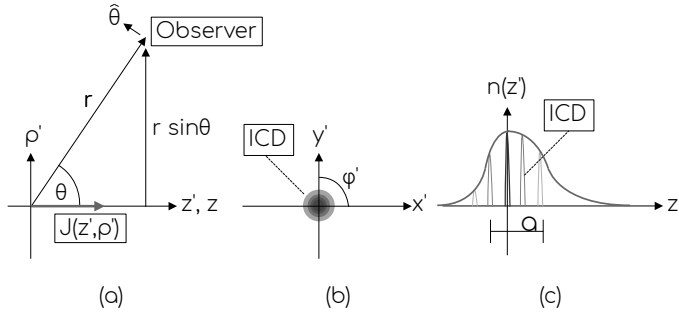


FIG. 1: (a) Side view of the coordinate systems used in the analysis. Coordinates without primes are from a spherical system and refer to the observer. Primed coordinates refer to the reference frame of the vector current density, $\vec{J}(\rho', z')$, and are from a cylindrical system. (b) Front view of the coordinate system. The instantaneous charge density (ICD) is assumed to have cylindrical symmetry with no ϕ' -dependence. (c) The function $n(z')$ describes the total cascade excess charge, and it has a characteristic width a . At any given moment, the ICD has a width much smaller than a [20].

In Figure 1 (c), an archetypal cascade profile is shown in the form of an *excess* charge function $n(z')$ with characteristic longitudinal length a . The individual ICDs represent the excess charge density in moments in time, whereas $n(z')$ refers to the excess charge as a function of $z' = ct'$. Approximating the central portion of $n(z')$ as a Gaussian distribution $N(\mu, \sigma)$ corresponds to setting $a = 2\sigma$. Askaryan radiation occurs because of the excess charge from cascade electrons ($\approx 20\%$), an effect verified by ZHS and later with GEANT4 [13, 20, 33]. Cascades may be characterized as *electromagnetic*, initiated by charged outgoing leptons from the UHE- ν interaction, or *hadronic*, initiated by the nucleus with which the UHE- ν interacts. In fully analytic models, cascade profiles are given by the Greisen distribution (electromagnetic case) and the Gaisser-Hillas distribution (hadronic case). This is also true in MC codes like AraSim that utilize the semi-analytic ARVZ parameterization [11].

The units of the electromagnetic field in the Fourier domain are V/m/Hz, often converted in the literature to V/m/MHz. To make the distance-dependence explicit, both sides of field equations are multiplied by r , as in $r\vec{E} = \dots$, making the units V/Hz. Throughout this work, an overall field normalization constant E_0 is used *in the time domain*, and it is directly proportional to the cascade energy E_C , as in most Askaryan models that followed from the original full MC results [13]. Thus, E_0 may be linearly scaled with energy, provided the longitudinal length a and the maximum number of cascade particles are derived consistently from the appropriate cascade distribution. When the field amplitude is proportional to E_0 times a characteristic frequency-squared (on-cone), the units of E_0 must be V/Hz². When the field amplitude is proportional to E_0 times a characteristic frequency divided by a characteristic pulse width

(off-cone), the units of E_0 remain V/Hz².

It will be shown in Section III B that the longitudinal length a in both the electromagnetic and hadronic cases demonstrates a weak dependence on the ratio of the initial cascade energy to the cascade critical energy: $a \sim \sqrt{\ln(E_C/E_{\text{crit}})}$. Specifically for the Greisen distribution, it can be shown that if $n_{\text{max}} = n(z_{\text{max}})$, where $z_{\text{max}} = \ln(E_C/E_{\text{crit}})$, then $n_{\text{max}}a \sim E_C/E_{\text{crit}}$. Thus, the area under the curve $n(z')$ scales as E_C . Among the RB results is the idea that the Askaryan radiation amplitude is proportional to $n_{\text{max}}a$. Although the amplitude develops over a cascade of length a , the RB field equations remain valid for a coherence length $\Delta z'_{\text{coh}}$ in which $r(t)$ is stable to first order relative to a wavelength.

The η parameter is the square of the ratio of a to $\Delta z'_{\text{coh}}$:

$$\eta = \left(\frac{a}{\Delta z'_{\text{coh}}} \right)^2 = \frac{k}{r} (a \sin \theta)^2 \quad (1)$$

The dominant Askaryan radiation occurs when $|z'| \lesssim \Delta z'$. In far-field, $\eta < 1$. The calculations, however, are valid for any η , rather than only the in the far-field ($\eta \ll 1$, and $kr \ll 1$, $r \gg a$). If $a \ll \Delta z'_{\text{coh}}$, then the fields have spherical symmetry, and the limit $kr \gg 1$ corresponds to the far-field. Conversely, if $a \gg \Delta z'_{\text{coh}}$, and $kr \ll 1$, then $\eta \gg 1$ and the radiation is observed in the near-field. In the first JCH+AC model, a limiting frequency ω_C (Equation 2) was shown to filter the Askaryan radiation. The effect of ω_C on the Askaryan E-field is described in Section IV.

$$\eta = \frac{\omega}{\omega_C} \quad (2)$$

The Askaryan radiation is primarily polarized along the unit vector $\hat{\theta}$, although there is a small amount of amplitude along \hat{r} [20]. The wavevector associated with propagation along r and polarized linearly along $\hat{\theta}$ is $k = (2\pi)/(n\lambda)$, where n is the index of refraction. A 3D wavevector is defined by RB, equivalent to $\vec{q} = nk(1, \vec{\rho}/R)$. Let the vector current density be equal to the charge density times the velocity of the ICD: $\vec{J}(t, \vec{x}') = \rho(z' - vt, \rho')\vec{v}$. Further, the charge density is factored into charge times ICD as a number density: $\rho(z' - vt, \rho') = n(z')f(z' - vt, \rho')$. The form factor that filters the $\hat{\theta}$ -polarized radiation is the three-dimensional spatial Fourier transform of $f(z' - vt, \rho')$:

$$\tilde{F}(\vec{q}) = \int d^3x' f(x') e^{-i\vec{q} \cdot \vec{x}'} \quad (3)$$

The result for \tilde{F} was calculated by JCH+AC [20], and more detail on that derivation is provided in Section III A, along with the energy-dependence on the longitudinal length a in Section III B. One main result shown by JCH+AC is that the effect of \tilde{F} on the radiation is that

of a two-pole low-pass filter if $\sigma < 1$, where σ is the ratio of angular frequency to the cutoff frequency introduced by the form factor:

$$\sigma = \frac{\omega}{\omega_{\text{CF}}} \quad (4)$$

Armed with the form factor, the longitudinal length parameter, and the RB field equations, the main electromagnetic field may be assembled according to the following form:

$$r\vec{E}(\omega, \theta) = E_0 \left(\frac{\omega}{2\pi} \right) \psi \vec{\mathcal{E}}(\omega, \theta) \tilde{F}(\omega, \theta) \quad (5)$$

The factor E_0 represents the overall amplitude scale, and it is proportional to cascade energy. The factor ω is the angular frequency. The variable ψ is $\psi = -i \exp(ikr) \sin \theta$. The function $\vec{\mathcal{E}}(\omega, \theta)$ contains the vector and complex pole structure of the field (see [20]). As presented above, $\tilde{F}(\omega, \theta)$ is the form factor. Thus, the model represented by Equation 5 is an *all-θ, all-ω* model. Equation 5 is valid at all frequencies not attenuated by $\tilde{F}(\omega, \theta)$, and all viewing angles not attenuated by $\vec{\mathcal{E}}(\omega, \theta)$. The goal of the following sections is to build an *all-θ, all-t* model in the time-domain, derived from Equation 5.

III. THE FORM FACTOR AND LONGITUDINAL LENGTH PARAMETER

In order to arrive at the main electromagnetic field in the time-domain, the individual pieces of Equation 5 must first be assembled. The first piece will be the form factor \tilde{F} that accounts for the 3D ICD, followed by some remarks about the energy-dependence of the longitudinal length parameter a .

A. The Form Factor

Let an observer be a distance r from a charge distribution $f(z', \rho')$ in a primed cylindrical coordinate system $\vec{x}' = (z', \rho')$. Let the scalar wavevector in a material with index of refraction n be $k = 2\pi/(n\lambda)$, and the angular frequency be $\omega = ck$. Recall the definition of \vec{q} from Section II: $\vec{q} = nk(1, \vec{\rho}/R)$. As presented in Section II the *form factor* for the cascade ICD be the 3D Fourier transform of $f(z', \rho')$.

$$F(\vec{q}) = \int d^3x' f(z', \rho') e^{-i\vec{q}\cdot\vec{x}'} \quad (6)$$

The goal is to evaluate \tilde{F} in the Fourier domain for an ICD definition informed by cascade simulations. Simulations of the cascade induced by the neutrino indicate a thin wave of charge in z' spread uniformly in ϕ' , that decreases exponentially in ρ' [20]. Thus,

$$f(x') = \rho_0^2 \delta(z' - ct) \exp(-\sqrt{2\pi}\rho_0\rho') \quad (7)$$

The thin wave of charge moves at speed c , and the ρ_0 parameter has units of inverse length. The ICD function $f(z', \rho')$ is a number density that should be normalized to 1. Integrating over the volume element d^3x' gives

$$I = \int d^3x' \rho_0^2 \delta(z' - ct) \exp(-\sqrt{2\pi}\rho_0\rho') \quad (8)$$

$$I = \int_0^\infty \int_0^{2\pi} \rho' d\rho' d\phi' \rho_0^2 \exp(-\sqrt{2\pi}\rho_0\rho') \quad (9)$$

$$I = 2\pi\rho_0^2 \int_0^\infty \rho' d\rho' \exp(-\sqrt{2\pi}\rho_0\rho') \quad (10)$$

$$I = 2\pi\rho_0^2 \left(\sqrt{2\pi}\rho_0 \right)^{-2} = 1 \quad (11)$$

To begin the evaluation of \tilde{F} , the exponent $-i\vec{q}\cdot\vec{x}'$ must be expanded. Let $nk \rightarrow k$, and assume that k now refers to the scalar wavevector in the medium.

$$-i\vec{q}\cdot\vec{x}' = -ikz' - i\frac{k}{r}\rho\rho' \cos(\phi') \quad (12)$$

From the coordinate system, $\rho = r \sin(\theta)$, so

$$-i\mathbf{q}\cdot\mathbf{x}' = -ikz' - ik \sin(\theta) \rho' \cos(\phi') \quad (13)$$

Then we have for \tilde{F} :

$$\tilde{F} = \int_{-\infty}^\infty \int_0^\infty \int_0^{2\pi} dz' \rho' d\rho' d\phi' \rho_0^2 \delta(z' - ct) e^{-i\vec{q}\cdot\vec{x}' - \sqrt{2\pi}\rho_0\rho'} \quad (14)$$

Evaluating the z' integral and inserting Equation 13:

$$\tilde{F} = \int_0^\infty \int_0^{2\pi} \rho' d\rho' d\phi' \rho_0^2 e^{-ik \sin(\theta) \rho' \cos(\phi') - \sqrt{2\pi}\rho_0\rho'} \quad (15)$$

Two physical parameters are necessary to compare wavelength to lateral ICD width. First, let γ be the projected scalar wavevector, and σ be the ratio between γ and the slope of the ICD:

$$\gamma = k \sin(\theta) \quad (16)$$

$$\sigma = \gamma / (\sqrt{2\pi}\rho_0) \quad (17)$$

The integral becomes

$$\tilde{F} = \rho_0^2 \int_0^\infty \int_0^{2\pi} \rho' d\rho' d\phi' e^{-i\gamma\rho' \cos(\phi') - \frac{\gamma}{\sigma}\rho'} \quad (18)$$

Rearranging to perform the ϕ' -integral first:

$$\tilde{F} = \rho_0^2 \int_0^\infty d\rho' \rho' e^{-\frac{\gamma}{\sigma} \rho'} \int_0^{2\pi} d\phi' e^{-i\gamma\rho' \cos(\phi')} \quad (19)$$

The cylindrical symmetry of $f(\mathbf{x}')$ leaves one free to choose where $\phi' = 0$. Thus, the azimuthal angle $\phi' \rightarrow \phi' - \pi$ may be rotated, changing $-\cos(\phi')$ to $\cos(\phi')$:

$$\tilde{F} = \rho_0^2 \int_0^\infty d\rho' \rho' e^{-\frac{\gamma}{\sigma} \rho'} \int_{-\pi}^{\pi} d\phi' e^{i\gamma\rho' \cos(\phi')} \quad (20)$$

The ϕ' -integral is now proportional to one representation of the 0-th order Bessel function of the first kind:

$$2\pi J_0(\gamma\rho') = \int_{-\pi}^{\pi} d\phi' e^{i\gamma\rho' \cos(\phi')} \quad (21)$$

Substituting Equation 21 into Equation 20,

$$\tilde{F} = 2\pi\rho_0^2 \int_0^\infty d\rho' \rho' e^{-\frac{\gamma}{\sigma} \rho'} J_0(\gamma\rho') \quad (22)$$

Let $u' = \gamma\rho'$. This substitution yields

$$F = \sigma^{-2} \int_0^\infty du' u' e^{-u'/\sigma} J_0(u') \quad (23)$$

Let $p = \sigma^{-1}$. The integral may be completed using Abramowitz and Stegun 11.3.5 [34]:

$$\tilde{F} = p^2 \lim_{z \rightarrow \infty} g_{1,0}(z) \quad (24)$$

$$\lim_{z \rightarrow \infty} g_{1,0}(z) = p \lim_{z \rightarrow \infty} g_{0,0}(z) \quad (25)$$

$$\tilde{F} = \frac{p^3}{1 + p^2} \int_0^\infty e^{-pt} J_0(t) dt \quad (26)$$

$$\tilde{F} = \frac{p^3}{(1 + p^2)^{3/2}} \quad (27)$$

$$\tilde{F} = \frac{1}{(1 + \sigma^2)^{3/2}} \quad (28)$$

According to Equation 28, the form factor is a low-pass filter with the cutoff-frequency ω_{CF} introduced in Section II: $\sigma = \omega/\omega_{\text{CF}}$. In Figure 2, Equation 28 is graphed along with the following *two-pole approximation*, for $\sigma < 1$:

$$\tilde{F} = \frac{1}{(1 + \sigma^2)^{3/2}} \approx \frac{1}{1 + \frac{3}{2}\sigma^2} \quad (29)$$

$$\tilde{F} \approx \frac{1}{(1 + i\sqrt{3/2}\sigma)(1 - i\sqrt{3/2}\sigma)} \quad (30)$$

$$\tilde{F} \approx \frac{\omega_0^2}{(\omega + i\omega_0)(\omega - i\omega_0)} \quad (31)$$

The definition $\omega_0 = \sqrt{2/3} \omega_{\text{CF}}$ has been used in the final step. The two-pole approximation resembles the original ZHS parameterization that matched full MC results below 1 GHz (see Equation 20 of [13]).

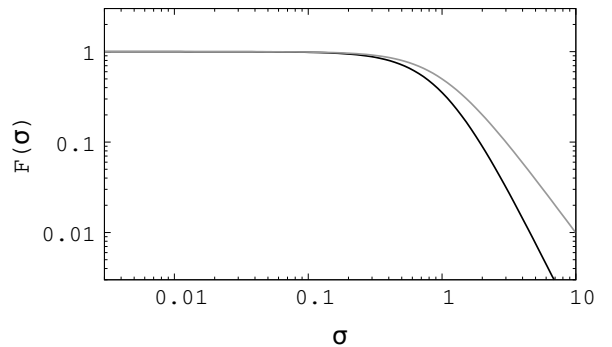


FIG. 2: (Black) Equation 28, graphed versus $\sigma = \omega/\omega_{\text{CF}}$. (Gray) The two-pole approximation.

1. A Note about the Molière Radius

In Section VI below, the parameter $l = 1/(\sqrt{2\pi}\rho_0)$ will be derived from best-fit ω_0 values. The parameter l is the decay constant of the exponential in the ICD (Equation 7). The l -parameter can vary because the best-fit ω_0 varies, and the two numbers are connected by Equation 4. It is important to note that $l \neq R_M$, where R_M is the constant Molière radius.

The Molière radius is defined as the lateral radius which forms a cylinder containing 90% of the energy deposition of a cascade in dense media. Let X_0 be the electromagnetic radiation length in ice, and let Z be the atomic number. A common formula for the Molière radius, R_M , is

$$R_M = 0.0265 X_0 (Z + 1.2) \quad (32)$$

Another useful formula relates X_0 to Z and the mass number A :

$$X_0 = 716.4 \text{ g cm}^{-2} \frac{A}{Z(Z + 1) \ln \left(\frac{287}{\sqrt{Z}} \right)} \quad (33)$$

Using $Z = 8$ and $A = 16$ for oxygen: $X_0 = 34.46 \text{ g cm}^{-2}$. Converting R_M to units of cm, 0.917 g cm^{-3} , gives $R_M = 9.16 \text{ cm}$. The measured value for water is 9.77 cm . Although it is tempting to compare l to R_M , these parameters have entirely different definitions. Knowing that l is related to ω_0 , l may be estimated as $\lambda/2$ at the cutoff-frequency in ice. At 3 GHz in ice, $\lambda/2 \approx 2.8 \text{ cm}$, and at 1 GHz in ice, $\lambda/2 \approx 8.4 \text{ cm}$. *Although the results are at the same order of magnitude as R_M , it will be shown that there are three effects limiting the high-frequency spectrum of the radiation: ω_0 , ω_{CF} , and the viewing angle.* Thus, l can be less than R_M and the radiation can still be limited to $\lesssim 1 \text{ GHz}$.

B. The Longitudinal Length Parameter

The next piece required in the assembly of the main electromagnetic field is the energy-dependence of the overall amplitude, and the energy dependence of the longitudinal length parameter, a . What follows are two separate discussions, one for electromagnetic cascades, and one for hadronic cascades.

1. Electromagnetic Case

The number of charged particles versus distance $n(z')$ in an electromagnetic cascade taking place in a dense medium with initial cascade energy E_C , critical energy E_{crit} , normalization parameter n_0 , and age s is [20]

$$n(z') = \frac{n_0}{\sqrt{\ln(E_C/E_{crit})}} \exp \left\{ z' \left(1 - \frac{3}{2} \ln(s) \right) \right\} \quad (34)$$

The age is given by

$$s = \frac{3z'}{z' + 2 \ln(E_C/E_{crit})} \quad (35)$$

The function $n(z')$ is known as the Greisen distribution. In this case, the longitudinal distance variable z' is in radiation lengths, and $n(z')$ is maximized at $z'_{max} = \ln(x)$, where $x = E_C/E_{crit}$. The calculation of the energy dependence of a is broken into four steps: normalization of $n(z')$ to be a fraction of the maximum, n_{max} , conversion of $n(z')$ to $n(s)$, determination of the width of $n(s)$, and conversion of the width in s to a width in z' .

Substituting $s = 1$ and $z' = \ln(x)$ into $n(z')$ yields n_{max} :

$$n_{max} = \frac{n_0 x}{\sqrt{\ln(x)}} \quad (36)$$

Dividing $n(z')$ by n_{max} yields

$$f(z') = x^{-1} \exp \left\{ z' \left(1 - \frac{3}{2} \ln(s) \right) \right\} \quad (37)$$

The function $f(z')$ is the normalized Greisen distribution. Solving the age equation for z' :

$$z' = \frac{2s \ln(x)}{3 - s} \quad (38)$$

From this point forward, since $f(z')$ is being studied near $s = 1$, we use $\ln(s) \approx s - 1$. Substituting back into Equation 37:

$$f(s) = x^{-1} \exp \left\{ s \ln(x) \left(\frac{5 - 3s}{3 - s} \right) \right\} \quad (39)$$

To calculate the Gaussian width of $f(s)$, consider the following procedure. Suppose there is a function $f(y)$ such that $\ln(f(y))$ is equal to a negatively oriented quadratic: $\ln(f(y)) = -(1/2)y^2/\sigma^2$. Solving for y yields $y_{\pm} = \pm\sqrt{-2\ln f\sigma}$. Assuming $f(y)$ behaves like a Gaussian near the global maximum, the width is $\Delta y = y_+ - y_- = 2\sqrt{-2\ln f\sigma}$ and $\ln f = -0.5$ precisely when it should: $y = \sigma$. In a similar fashion, let $q = \ln(xf)/\ln(x)$ in Equation 39. This leaves

$$q = \frac{5 - 3s}{3 - s} s \quad (40)$$

Letting $b = (q + 5)/3$,

$$0 = q - bs + s^2 \quad (41)$$

$$s_{\pm} = \frac{b}{2} \pm \frac{1}{2} \sqrt{b^2 - 4q} \quad (42)$$

$$\Delta s = s_+ - s_- = \sqrt{b^2 - 4q} \quad (43)$$

The longitudinal length $\Delta z'$ is required. The conversion of Equation 43 can be made using Equation 38. The result is

$$\Delta z' = 2 \ln(x) \left(\frac{s_+}{3 - s_+} - \frac{s_-}{3 - s_-} \right) \quad (44)$$

The expression for $\Delta z'$ may be simplified using the definitions of s_{\pm} , q , and b :

$$\Delta z' = \frac{1}{2} \ln(x) (q^2 - 26q + 25)^{1/2} \quad (45)$$

Noting that $q = 1 + \ln(f)/\ln(x)$, and that the quadratic factors:

$$\Delta z' = \frac{1}{2} \ln(x) (q - 1)^{1/2} (q - 25)^{1/2} \quad (46)$$

$$\Delta z' = \frac{1}{2} \ln(x) (\ln(f)/\ln(x))^{1/2} (q - 25)^{1/2} \quad (47)$$

$$\Delta z' = \frac{1}{2} \sqrt{\ln(x)} (\ln(f) \ln(f)/\ln(x) - 24 \ln(f))^{1/2} \quad (48)$$

The term involving $(\ln(f))^2$ is small, positive, and negligible compared to the second term in that square root. Dropping it and setting $\Delta z' = a$ yields the main result:

$$a = \sqrt{\ln(x)} (-6 \ln(f))^{1/2} \quad (49)$$

Equation 49 is in radiation lengths. In solid ice the density is $\rho_{ice} = 0.917 \text{ g cm}^{-3}$, and the electromagnetic

radiation length is $z_0 = 36.08 \text{ g cm}^{-2}$ [20]. Converting to distance gives

$$a = \frac{z_0}{\rho_{ice}} \sqrt{\ln(x)} \sqrt{-6 \ln(f)} \quad (50)$$

Note that $a \propto \sqrt{\ln(x)}$. Since $n_{\max} \propto x/\sqrt{\ln(x)}$, the product $n_{\max}a$, is an approximation of the area under $n(z')$, and it goes as the energy $x = E_C/E_{\text{crit}}$. This was noted by RB [31], who placed $n_{\max}a$ in the electromagnetic field normalization rather than E_C . Allowing f to drop to 40% of its peak value, and using $E_{\text{crit}} \approx 10^8 \text{ eV}$, gives $a \approx 4 \text{ m}$ for $E_C = 10^{16} \text{ eV}$. It will be shown in Section VI that 4 meters is a good number for a 10^{16} eV cascade derived from full MC simulations.

2. Hadronic Case

The Gaisser-Hillas distribution describes hadronic cosmic-ray air showers, but has also been applied to hadronic cascades in dense media [22]. The original function reads

$$n(z') = N_{\max} \left(\frac{z' - z_0}{z_{\max} - z_0} \right)^{(z_{\max} - z_0)/\lambda} e^{\frac{z_{\max} - z'}{\lambda}} \quad (51)$$

The variables are defined as follows: N_{\max} is the instantaneous maximum number of particles in the cascade, z' is the longitudinal distance in radiation lengths, z_0 is the initial starting point, λ is the interaction length, and z'_{\max} is the location of N_{\max} .

The calculation of the energy dependence of a is broken into three steps: the normalization of $n(z')$ to be a fraction of n_{\max} with convenient parameters, approximation the distribution near z_{\max} , and the longitudinal width determination that contains a pre-defined fraction of the normalized n_{\max} . Let $x = (z' - z_0)/\lambda$, and $w = (z_{\max} - z_0)/\lambda$. One useful (normalized) parameterization is

$$f(z') = \left(\frac{x}{w} \right)^w \exp(w - x) \quad (52)$$

Taking the logarithm of both sides of Eq. 52 and then dividing both sides by w gives:

$$\frac{\ln(f)}{w} = \ln(x/w) + 1 - \frac{x}{w} \quad (53)$$

Near the shower maximum, $x/w \approx 1$. Let $\epsilon = x/w$, and expand the right-hand side in a series about $\epsilon = 1$ to second order, noting that the first order vanishes:

$$\frac{\ln(f)}{w} = -\frac{1}{2}(\epsilon - 1)^2 \quad (54)$$

Notice that the logarithm of the normalized distribution is again a negative quadratic, indicating Gaussian behavior near z'_{\max} . Let $b = \ln(f)/w$, and solve the quadratic equation for ϵ :

$$0 = \epsilon^2 - 2\epsilon + 1 + 2b \quad (55)$$

As with the electromagnetic case, let $\Delta\epsilon = \epsilon_+ - \epsilon_-$, where ϵ_+ and ϵ_- are the two solutions to the quadratic. The result is

$$\Delta\epsilon = 2\sqrt{-2b} \quad (56)$$

Assuming constant density, the starting point of the cascade z_0 is arbitrary, so z_0 may be set to zero. Also, $\Delta x = w\Delta\epsilon$, so

$$\Delta x = \sqrt{w} \sqrt{-8 \ln(f)} \quad (57)$$

If $z_0 = 0$, $w = z'_{\max}/\lambda$. Finally, knowing that $\Delta z' = \lambda\Delta x$, the result becomes

$$a = \Delta z' = \sqrt{\lambda z'_{\max}} \sqrt{-8 \ln(f)} \quad (58)$$

As with the electromagnetic case, the longitudinal length parameter a goes as $\sqrt{z_{\max}}$.

IV. ON-CONE FIELD EQUATIONS

The $\hat{\theta}$ -component of the electromagnetic field at $\theta = \theta_C$ will now be built in the time-domain, using the general RB field equations in the Fourier domain, along with the form factor and longitudinal length parameter. Beginning with Eq. 45 JCH+AC [20], assuming Equation 28 for the form factor, with $\sigma = \omega/\omega_{\text{CF}}$ and $\eta = \omega/\omega_{\text{CF}}$, and letting $E_0 = E_C \approx n_{\max}a$:

$$r\tilde{E}(\omega, \theta_C) = \frac{(-i\omega)E_0 \sin(\theta_C) e^{i\omega R/c}}{(1 - i\omega/\omega_C)^{1/2} (1 + (\omega/\omega_{\text{CF}})^2)^{3/2}} \quad (59)$$

Suppose $\omega < \omega_C$, and $\omega < \omega_{\text{CF}}$, such that the following approximations are valid:

$$(1 - i\omega/\omega_C)^{1/2} \approx 1 - \frac{i}{2} \frac{\omega}{\omega_C} \quad (60)$$

$$(1 + (\omega/\omega_{\text{CF}})^2)^{3/2} \approx 1 + \frac{3}{2} \left(\frac{\omega}{\omega_{\text{CF}}} \right)^2 \quad (61)$$

Using the approximations introduces simple poles into the complex formula for the frequency-dependent electric field.

Inserting the approximations in the denominator of Eq. 5, we have

$$r\tilde{E}(\omega, \theta_C) = \frac{(-i\omega)E_0 \sin(\theta_C)e^{i\omega R/c}}{(1 - \frac{i}{2}\omega/\omega_C)(1 + \frac{3}{2}(\omega/\omega_{CF})^2)} \quad (62)$$

The denominator can be rearranged by factoring the ω coefficients, and defining $\omega_0 = \sqrt{\frac{2}{3}}\omega_{CF}$.

$$r\tilde{E}(\omega, \theta_C) = \frac{2i\omega_C\omega_0^2(-i\omega)E_0 \sin(\theta_C)e^{i\omega r/c}}{(2i\omega_C + \omega)(\omega + i\omega_0)(\omega - i\omega_0)} \quad (63)$$

Let $\hat{E}_0 = E_0 \sin(\theta_C)$, and let the retarded time be $t_r = t - r/c$. Taking the *inverse* Fourier transform, using the same Fourier sign convention as RB [31] ($f(t) = (2\pi)^{-1} \int_{-\infty}^{\infty} \tilde{F}(\omega)e^{-i\omega t} d\omega$),

$$rE(t, \theta_C) = \frac{\hat{E}_0 i\omega_C \omega_0^2}{\pi} \frac{d}{dt_r} \int_{-\infty}^{\infty} \frac{e^{-i\omega t_r}}{(2i\omega_C + \omega)(\omega + i\omega_0)(\omega - i\omega_0)} d\omega \quad (64)$$

In Equation 64, the derivative with respect to the retarded time d/dt_r is introduced to remove a factor of $(-i\omega)$ from the numerator. Equation 64 has three poles, all on the imaginary axis. Convergence of Eq. 64 depends on the sign of the retarded time. Each case is now considered separately.

1. If $t_r > 0$: Consider the contour comprised of the real axis and the clockwise-oriented negative infinite semi-circle. On the contour, the exponential phase factor in Eq. 64 goes as

$$\exp(-i\omega t_r) = \exp(-i(R \cos \phi + iR \sin \phi)t_r) \quad (65)$$

For the semi-circle, $\phi \in [\pi, 2\pi]$, so $\sin \phi < 0$ and $t_r > 0$. Exponential decay occurs and the integrand vanishes on the semi-circle for $|\omega| = R \rightarrow \infty$.

2. If $t_r < 0$: Consider the contour comprised of the real axis and the counter-clockwise-oriented positive infinite semi-circle. On the contour, the exponential phase factor in Eq. 64 goes again as

$$\exp(-i\omega t_r) = \exp(-i(R \cos \phi + iR \sin \phi)t_r) \quad (66)$$

For the semi-circle, $\phi \in [0, \pi]$, so $\sin \phi > 0$ and $t_r < 0$. Exponential decay occurs and the integrand vanishes on the semi-circle for $|\omega| = R \rightarrow \infty$.

Using cases 1 and 2, Equation 64 can be solved using the Cauchy integral formula. Beginning with $t_r > 0$, two poles are enclosed in the semi-circle: one that originated from the coherence cutoff frequency, and the other that originated from the form factor. The Cauchy integral formula yields

$$rE(t, \theta_C) = 2\hat{E}_0 \omega_C \omega_0^2 \frac{d}{dt_r} \left(\frac{e^{-2\omega_C t_r}}{i^2(-2\omega_C + \omega_0)(-2\omega_C - \omega_0)} + \frac{e^{-\omega_0 t_r}}{i^2(-\omega_0 + 2\omega_C)(-2\omega_0)} \right) \quad (67)$$

Define the ratio of the cutoff frequencies: $\epsilon = \omega_0/\omega_C$. After evaluating the time derivatives, Equation 67 becomes

$$rE(t, \theta_C) = \hat{E}_0 \omega_0^2 \left(\frac{e^{-2\omega_C t_r}}{(1 - \frac{\epsilon}{2})(1 + \frac{\epsilon}{2})} - \frac{e^{-\omega_0 t_r}}{(2)(1 - \frac{\epsilon}{2})} \right) \quad (68)$$

Expanding to linear order in ϵ , assuming $\epsilon < 1$, and recalling that $\omega_0^2 = \frac{2}{3}\omega_{CF}^2$:

$$rE(t, \theta_C) \approx \frac{1}{3} \hat{E}_0 \omega_{CF}^2 \left(2e^{-2\omega_C t_r} - \left(1 + \frac{\epsilon}{2} \right) e^{-\omega_0 t_r} \right) \quad (69)$$

Turning to the case of $t_r < 0$, consider integrating Eq. 64 along the contour comprised of the real axis and the counter-clockwise-oriented positive infinite semi-circle. The contour encloses one pole, and the exponent ensures convergence:

$$rE(t, \theta_C) = (2\pi i) \hat{E}_0 (\pi)^{-1} i\omega_C \omega_0^2 \frac{d}{dt_r} \left(\frac{e^{\omega_0 t_r}}{(2i\omega_C + i\omega_0)(2i\omega_0)} \right) \quad (70)$$

After evaluating the derivative, the expression simplifies with $\epsilon = \omega_0/\omega_C$:

$$rE(t, \theta_C) = \frac{1}{2} \hat{E}_0 \omega_0^2 \left(\frac{e^{\omega_0 t_r}}{1 + \frac{1}{2}\epsilon} \right) \quad (71)$$

Finally, using the same first-order approximation in ϵ as the $t_r > 0$ case:

$$rE(t, \theta_C) \approx \frac{1}{3} \hat{E}_0 \omega_{CF}^2 \left(1 - \frac{1}{2}\epsilon \right) e^{\omega_0 t_r} \quad (72)$$

Collecting the $t_r > 0$ and $t_r < 0$ results together:

$$rE(t, \theta_C) = \frac{1}{3} \hat{E}_0 \omega_{CF}^2 \begin{cases} \left(1 - \frac{1}{2}\epsilon \right) e^{\omega_0 t_r} & t_r < 0 \\ \left(2e^{-2\omega_C t_r} - \left(1 + \frac{\epsilon}{2} \right) e^{-\omega_0 t_r} \right) & t_r > 0 \end{cases} \quad (73)$$

Parameter	Definition
\hat{E}_0	$E_0 \sin(\theta_C)$
E_0	$\approx n_{max}a$
ω_0	$\sqrt{\frac{2}{3}}\omega_{CF}$
ω_{CF}	$(c\sqrt{2\pi}\rho_0)/(n \sin \theta)$
ω_C	$(rc)/(na^2 \sin^2 \theta)$
$\epsilon = \omega_0/\omega_C$	$\sqrt{2/3}(\sqrt{2\pi}\rho_0a)(a/r)$ (see Eq. 46 of [20])
t_r	$t - r/c$

TABLE I: The parameters used to build Equation 73. Fitted values in comparison to semi-analytic parameterizations are shown in Section VI.

Equation 73 represents the time-domain solution for the on-cone $\hat{\theta}$ -component of the Askaryan electric field. Table I summarizes the definitions of the parameters in Equation 73. Fit results for the parameters of Table I are shown in Section VI.

Notice that the overall field amplitude scales with energy ($E_0 \propto E_C \sim n_{max}a$) and with the second power of cutoff-frequency. The units of E_0 are therefore V Hz². The amplitude is asymmetric, and the parameter ϵ influences the asymmetry. The ϵ parameter was studied in JCH+AC in detail. For example, Figure 10 of [20] shows that $\epsilon \approx [0.1 - 1]$ for $\sqrt{2\pi}\rho_0 \approx 20$ m⁻¹ and $a \approx 4$ m. These values are typical of 10 PeV cascades (see Section VI). The expression for ϵ is the product of the ratio of the lateral to longitudinal length, and the longitudinal length to the vertex distance, making it a physical parameter connecting the event geometry to the cascade shape. Figure 3 displays normalized examples of Equation 73 for different values of ϵ .

A. Verification of the Uncertainty Principle

Among the results of JCH+AC is the Gaussian width of the radiation in the Fourier domain: σ_ν , where ν rep-

resents the frequency. Generally speaking, the product of the width in the Fourier domain with the width in the time domain must be greater than or equal to some constant. Gaussian functions minimize this *uncertainty principle*. The following procedure is used to compute the width σ_t of the on-cone field. First, the branches corresponding to $t_r < 0$ and $t_r > 0$ are each treated as probability distribution functions, and normalized. Next the average positive and negative retarded times, $\bar{t}_{r,+}$ and $\bar{t}_{r,-}$, are computed:

$$\bar{t}_{r,+} = \frac{\omega_0}{\frac{1}{2}\epsilon - 1} \int_0^\infty 2t_r e^{-2\omega_C t_r} - \left(1 + \frac{1}{2}\epsilon \right) t_r e^{-\omega_0 t_r} dt_r \quad (74)$$

$$\bar{t}_{r,-} = \omega_0 \int_{-\infty}^0 t_r e^{\omega_0 t_r} dt_r \quad (75)$$

Subtracting the two averages yields σ_t , which simplifies to

$$\sigma_t = \bar{t}_{r,+} - \bar{t}_{r,-} = \frac{\epsilon + 2}{\omega_0} = \frac{1}{\omega_C} + \frac{2}{\omega_0} \quad (76)$$

The result has the correct units and the limiting cases are sensible. Suppose $\epsilon \rightarrow 0$ ($\omega_C \gg \omega_0$), then $\sigma_t \rightarrow 2/\omega_0$, which is expected from observing Equation 73 if the ω_C exponential disappears. If $\epsilon = 1$ ($\omega_C = \omega_0$), then $\sigma_t = 3/\omega_0$. That is, the pulse is wider if there is more than one relevant cutoff frequency. The result also reveals that as the pulse asymmetry grows with ϵ , so does the pulse width.

Equation 36 of JCH+AC [20] provides σ_ν :

$$\sigma_\nu = \frac{c}{2\pi a \Delta \cos \theta} (1 + \eta^2)^{1/2} \quad (77)$$

Expanding to first order in $\Delta \cos(\theta) = \cos(\theta) - \cos(\theta_C)$,

$$\sigma_\nu \approx \frac{c}{2\pi a \sin(\theta_C) \Delta \theta} (1 + \eta^2)^{1/2} \quad (78)$$

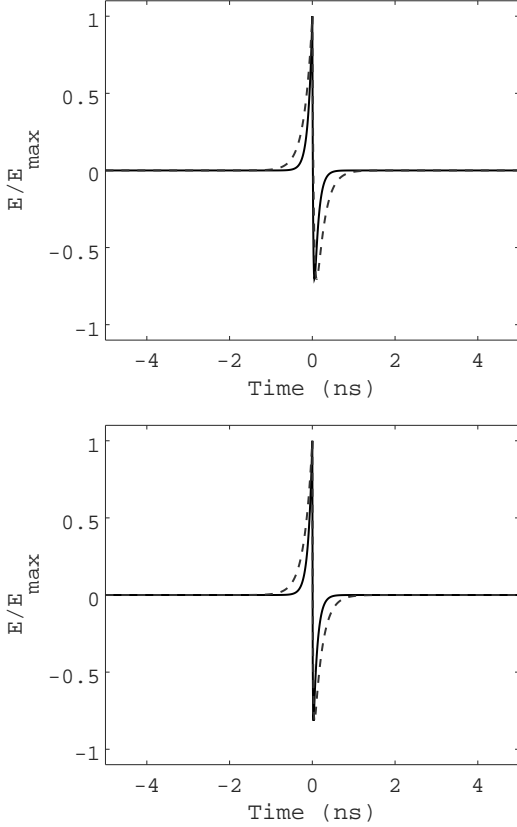


FIG. 3: $E(t, \theta_C)$ vs. t_r (Equation 73), normalized. Top: (Solid black) $\omega_{CF}/(2\pi) = 2.0$ GHz, $\omega_C/(2\pi) = 4.0$ GHz, $\epsilon = 0.5$. (Dashed black) $\omega_{CF}/(2\pi) = 1.0$ GHz, $\omega_C/(2\pi) = 2.0$ GHz, $\epsilon = 0.5$. Bottom: (Solid black) $\omega_{CF}/(2\pi) = 2.0$ GHz, $\omega_C/(2\pi) = 10.0$ GHz, $\epsilon = 0.2$. (Dashed black) $\omega_{CF}/(2\pi) = 1.0$ GHz, $\omega_C/(2\pi) = 5.0$ GHz, $\epsilon = 0.2$. All field functions are normalized to the maximum positive value.

From previous definitions, let $\omega_C^{-1} = a^2 \sin^2(\theta_C)/(rc)$, and $\omega_0^{-1} = l \sin(\theta_C)/c$, where $l = \sqrt{3/2}/(\sqrt{2\pi}\rho_0)$. Noting that $\sigma_t = \omega_C^{-1} + 2\omega_0^{-1}$, the uncertainty product is

$$\sigma_\nu \sigma_t = \frac{1}{2\pi} \left(\left(\frac{a}{r} \right) \frac{\sin(\theta_C)}{\Delta\theta} + \sqrt{6} \left(\frac{l}{a} \right) \frac{1}{\Delta\theta} \right) (1 + \eta^2)^{1/2} \quad (79)$$

The limits $r \gg a$ and $ka \ll 1$ cause $\eta \rightarrow 0$. Assume these limits to be true, along with $\Delta\theta \rightarrow 0$. The result is

$$\sigma_\nu \sigma_t = \frac{1}{2\pi} \left(\left(\frac{a}{r} \right) \frac{\sin(\theta_C)}{\Delta\theta} + \sqrt{6} \left(\frac{l}{a} \right) \frac{1}{\Delta\theta} \right) \quad (80)$$

Therefore, in order to satisfy $\sigma_\nu \sigma_t > 1/(2\pi)$,

$$\left(\frac{a}{r} \right) \sin(\theta_C) + \sqrt{6} \left(\frac{l}{a} \right) > \Delta\theta \quad (81)$$

Although $a/r \ll 1$ and $l/a \ll 1$, as long as these expressions do not approach zero as fast as $\Delta\theta \rightarrow 0$ in Equation 81, the uncertainty principle holds. Yet these are

Variable	Definition
u	$1 - i\eta$
x	$\cos(\theta)$
x_C	$\cos(\theta_C)$
$\sin^2(\theta)$	$1 - x^2$
q	$(x^2 - xx_C)/(1 - x^2)$
y	$(\frac{1}{2})(ka)^2(\cos\theta - \cos\theta_C)^2$
p	$\frac{1}{2} \left(\frac{a}{c} \right)^2 (\cos(\theta) - \cos(\theta_C))^2$

TABLE II: Useful variables for the derivation of the off-cone Askaryan electromagnetic field.

exactly the conditions of the problem. The observer distance r is assumed to be in the far-field and much larger than the longitudinal length, and at cascade energies at or above 10 PeV, the longitudinal length is computed to be much larger than the lateral ICD width. Thus, the result is that $\sigma_\nu \sigma_t > 1/(2\pi)$.

V. OFF-CONE FIELD EQUATIONS

Turning to the case for which $\theta \neq \theta_C$, the $\hat{\theta}$ -component of the electromagnetic field will now be built in the time-domain. The RB field equations for the $\hat{\theta}$ and \hat{r} components are summarized in both RB and JCH+AC [20, 31]. Recall the general form of the electromagnetic field, given in Equation 5:

$$r \vec{E}(\omega, \theta) = E_0 \left(\frac{\omega}{2\pi} \right) \psi \vec{\mathcal{E}}(\omega, \theta) \tilde{F}(\omega, \theta) \quad (82)$$

The first task is to simplify $\vec{\mathcal{E}}(\omega, \theta)$ before taking the inverse Fourier transform. The simplification involves expanding $\vec{\mathcal{E}}(\omega, \theta)$ in a Taylor series such that $u = 1 - i\eta \approx 1$, restricting $\eta < 1$. The restriction $\eta < 1$ may be satisfied by either $a \sin \theta / r \ll 1$, or $ka \sin \theta \ll 1$, or both. Once $\vec{\mathcal{E}}(\omega, \theta)$ is simplified, the inverse Fourier transform of Equation 82 may be evaluated to produce the result. Table II contains useful variable definitions, Table III contains useful function definitions, and Table IV contains special cases of the functions in Table III.

Using the definitions in Tables II-IV, $\vec{\mathcal{E}}(u, x) \cdot \hat{\theta} = \mathcal{E}(u, x)$ near $u = 1$ gives

$$\mathcal{E}(u, x) = \mathcal{E}(x, 1) + (u - 1) \dot{\mathcal{E}}(x, 1) + \mathcal{O}(u - 1)^2 \quad (83)$$

The first term is $fg(1-h)$ evaluated at $u = 1$: $\exp(-y)$ (Table IV). The second term requires the first derivative of $\mathcal{E}(u, x)$ with respect to u , evaluated at $u = 1$.

$$\dot{\mathcal{E}}(u, x) = f\dot{g} + \dot{f}g - (fgh + f\dot{g}h + \dot{f}gh) \quad (84)$$

$$\dot{\mathcal{E}}(u, 1) = (f\dot{g} + \dot{f}g - (fgh + f\dot{g}h + \dot{f}gh))|_{u=1} \quad (85)$$

Function	Definition
$f(u, x)$	$\left(u + 3 \frac{(1-u)^2}{u} \frac{x^2 - x x_C}{1-x^2}\right)^{-1/2}$
$g(u, x)$	$\exp(-\frac{1}{2}(ka)^2(x - x_C)^2 u^{-1})$
$h(u, x)$	$\left(\frac{1-u}{u}\right) \left(\frac{x x_C - x^2}{1-x^2}\right)$
$\vec{\mathcal{E}}(u, x) \cdot \hat{\theta}$	$f(x, u)g(x, u)(1 - h(u, x))$

TABLE III: Useful functions for the derivation of the off-cone Askaryan electromagnetic field. The last row contains the vector structure of the $\hat{\theta}$ -component of the field.

Function ($u = 1$)	Result
$f(x, 1)$	1
$g(x, 1)$	$\exp(-y)$
$h(x, 1)$	0

TABLE IV: Special cases of the functions defined in Table III, when $u = 1$.

The first-derivatives of f , g , and h , evaluated at $u = 1$, are

$$\dot{f}|_{u=1} = -\frac{1}{2} \quad (86)$$

$$\dot{g}|_{u=1} = y \exp(-y) \quad (87)$$

$$\dot{h}|_{u=1} = q \quad (88)$$

Because $h(x, 1) = 0$, terms in Eq. 84 proportional to

h will vanish. Three terms remain, which are

$$\dot{\mathcal{E}}(u, 1) = y e^{-y} - \frac{1}{2} e^{-y} - e^{-y} q \quad (89)$$

$$\dot{\mathcal{E}}(u, 1) = \frac{1}{2} e^{-y} (2y - 2q - 1) \quad (90)$$

Inserting Eq. 90 into Eq. 83,

$$\mathcal{E}(x, u) \approx e^{-y} + (u - 1) \left(\frac{1}{2} e^{-y} (2y - 2q - 1) \right) \quad (91)$$

$$\mathcal{E}(x, u) = e^{-y} \left(1 + \frac{1}{2}(u - 1)(2y - 2q - 1) \right) \quad (92)$$

Using the definition of u (Table II), the result may be written

$$\mathcal{E}(x, u) = e^{-y} \left(1 - \frac{1}{2} j \eta (2y - 2q - 1) \right) \quad (93)$$

Proceeding with the inverse Fourier transform of the $\hat{\theta}$ -component:

$$rE(t, \theta) = \mathcal{F}^{-1} \left\{ E_0 \left(\frac{\omega}{2\pi} \right) \tilde{F} \psi \mathcal{E} \right\} \quad (94)$$

Inserting the Taylor series for \mathcal{E} and following the usual steps produces

$$2\pi rE(t, \theta) = \frac{E_0 \omega_0^2 \sin(\theta)}{2\pi} \frac{d}{dt_r} \int_{-\infty}^{\infty} \frac{e^{-i\omega t_r} e^{-y} (1 - \frac{1}{2} i\eta(2y - 2q - 1))}{(\omega + i\omega_0)(\omega - i\omega_0)} d\omega \quad (95)$$

Using $\eta = \omega/\omega_C$, $y = p\omega^2$ (Table II), and rearranging:

$$2\pi rE(t, \theta) = \frac{E_0 \omega_0^2 \sin(\theta)}{4\pi i\omega_C} \frac{d}{dt_r} \int_{-\infty}^{\infty} \frac{e^{-i\omega t_r - p\omega^2} (2i\omega_C + 2p\omega^3 - (2q + 1)\omega)}{\omega^2 + \omega_0^2} d\omega \quad (96)$$

Unlike the on-cone case, Equation 96 cannot be integrated with infinite semi-circle contours, because the exponential term diverges along the imaginary axis far from the origin. Let I_0 represent the constant term with respect to ω in the numerator:

$$I_0 = \int_{-\infty}^{\infty} \frac{e^{-i\omega t_r - p\omega^2} (2i\omega_C)}{\omega^2 + \omega_0^2} d\omega \quad (97)$$

Further, let I_1 and I_3 represent the linear and cubic terms, respectively. Completing the square in the exponent of I_0 , with $\omega_1 = t_r/(2p)$, yields

$$I_0 = 2i\omega_C e^{-\frac{t^2}{2p}} \int_{-\infty}^{\infty} \frac{e^{-p(\omega+i\omega_1)^2}}{\omega^2 + \omega_0^2} d\omega \quad (98)$$

Performing a substitution in the exponent reveals that I_0 involves a *Voigt function*, sometimes re-cast as the *line-broadening function* (DLMF 7.19, [35]). Let $x = i(\omega_1/\omega_0)$, and $1/4s = p\omega_0^2$. The result is

$$I_0 = 2i \left(\frac{\omega_C}{\omega_0} \right) e^{-\frac{t^2}{2p}} U(x, s) \quad (99)$$

Voigt functions are not expressed analytically, but there are examples of approximate polynomial expansions [36]. A simpler approach is to note that, for situations relevant to the current problem, $\omega > \omega_1$. Requiring that $\omega > \omega_1$ amounts to a restriction on t_r :

$$|t_r| < 2\pi\nu \sin^2 \theta_C \left(\frac{a}{c} \right)^2 (\theta_{\min} - \theta_C)^2 \quad (100)$$

In Equation 100, ν is the frequency, a is the longitudinal cascade length, θ_C is the Cherenkov angle, and θ_{\min} is the minimum viewing angle. For example, taking $a = 4.5$ meters and $\nu \approx 3$ GHz (appropriate for ν_{CF} , the form factor cutoff frequency), and letting $\Delta\theta$ be as small as 1.5° allows $|t_r| \lesssim 2$ ns. In most Askaryan models, the field approaches zero outside this window. Hereafter, this approximating step will be called the *symmetric approximation*.

$$I_0 \approx 2i\omega_C e^{-\frac{t^2}{2p}} \int_{-\infty}^{\infty} \frac{e^{-p\omega^2}}{\omega^2 + \omega_0^2} d\omega \quad (101)$$

Similar to integral representations of Voigt functions, the result for I_0 involves the complementary error function (DLMF 7.7.1, [35]):

$$I_0 = 2i\omega_C e^{-\frac{t^2}{2p}} \pi \omega_0^{-1} e^{p\omega_0^2} \text{erfc}(\sqrt{p}\omega_0) \quad (102)$$

One advantage of the symmetric approximation is that $I_1 = I_3 = 0$. These are odd integrals over $(-\infty, \infty)$, and only the contribution from I_0 remains. Inserting I_0 into Equation 96 and evaluating the derivative yields the result:

$$rE(t, \theta) = -\frac{E_0 \omega_0 \sin(\theta)}{8\pi p} t_r e^{-\frac{t_r^2}{4p} + p\omega_0^2} \text{erfc}(\sqrt{p}\omega_0) \quad (103)$$

Equation 103 represents the time-domain solution for the off-cone $\hat{\theta}$ -component of the Askaryan electric field. Equation 103 is graphed in Figures 4 and 5. In Figure 4 (top), $E(t, \theta)$ is shown normalized to the maximum value for the angular range displayed, $[\theta_C + 1.5^\circ, \theta_C + 5.5^\circ]$,

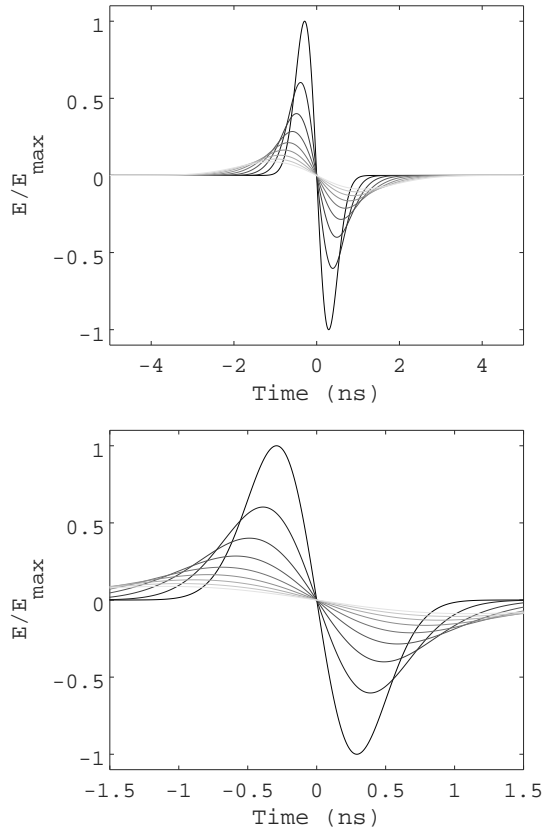


FIG. 4: $E(t, \theta)$ vs. t_r (Equation 103), normalized. The viewing angle θ is varied from $\theta_C + 1.5^\circ$ to $\theta_C + 5.5^\circ$ in steps of 0.5° . Top: $\omega_0/(2\pi) = 1.0$ GHz. Bottom: Same as top, zoomed in on central region.

from $t = [-5, 5]$ ns. Pulses with viewing angles closer to θ_C have larger relative amplitudes and shorter pulse widths. Figure 4 (bottom) contains the same results, but for $t = [-1.5, 1.5]$ ns. The pulses are symmetric and all zero crossings are at $t_r = 0$ ns, a result of the symmetric approximation. Figure 5 contains contours of the same results as in Figure 4. Table I summarizes the definitions of the parameters in Equation 103. Fit results for the parameters of Table I are shown in Section VI.

As in the on-cone result, the overall field amplitude scales with energy ($n_{\max}a$). However, the amplitude scales with the first power of cutoff-frequency. The units of E_0 remain V Hz² because of the factors of t_r and p , which have units of time and time-squared, respectively. Thus, the argument of the complementary error function, $\sqrt{p}\omega_0$, is unitless. This factor is strictly positive, so the range of the complementary error function is $(0, 1)$. The factor $\sqrt{p}\omega_0$ cannot be zero without setting $\theta = \theta_C$, or setting $\omega_{\text{CF}} = 0$. Both cases are not allowed. Equation 103 represents the *off-cone* ($\theta \neq \theta_C$) solution, so $p \neq 0$. Another possibility is that $p = 0$ if $a = 0$, but this implies $E_0 = 0$. Further, $\omega_{\text{CF}} = 0$ would require cascade particles to have no lateral momentum, which is not physical. Therefore, $0 < \text{erfc}(\sqrt{p}\omega_0) < 1$.

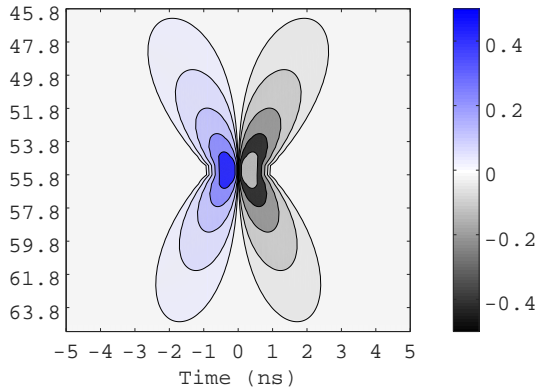


FIG. 5: Contours of $E(t, \theta)$ vs. θ vs. t_r (Equation 103), normalized. The normalization is the same as Figure 4. Although the contour lines extend into the region near θ_C , Equation 5 is only being evaluated at $\Delta\theta > 1.5^\circ$ (see text for details).

A. Verification of the Uncertainty Principle

As in Section IV A, the uncertainty principle should be checked. Equation 103 is an anti-symmetric Gaussian function with pulse width $\sigma_t = \sqrt{2p}$. Let $\Delta \cos \theta = (\cos \theta - \cos \theta_C)$. Using Table II, the expression $\sqrt{2p}$ evaluates to

$$\sigma_t = \sqrt{2p} = \left(\frac{a}{c}\right) (\Delta \cos \theta) \quad (104)$$

Recall that σ_ν is given by

$$\sigma_\nu = \frac{c}{2\pi a \Delta \cos \theta} (1 + \eta^2)^{1/2} \quad (105)$$

The uncertainty product is

$$\sigma_t \sigma_\nu = \frac{1}{2\pi} (1 + \eta^2)^{1/2} \quad (106)$$

In the limit that $\eta \rightarrow 0$ (the far-field), the uncertainty principle is minimized, as expected for Gaussian functions. Neither the time-domain result (Equation 103) nor the Fourier domain result from JCH+AC that generated Equation 77 are perfectly Gaussian. In the Fourier domain, the spectrum becomes linear near $\omega = 0$, and Equation 103 takes the Gaussian form, $x \exp(-x^2)$, as opposed to a pure Gaussian, $\exp(-x^2)$. Despite these subtleties, the main results of this work and JCH+AC obey the uncertainty principle.

VI. COMPARISON TO SEMI-ANALYTIC PARAMETERIZATIONS

The fully analytic model will now be compared to semi-analytic parameterizations used in NuRadioMC to pre-

dict observed signals in IceCube-Gen2 Radio. In principle, all semi-analytic models in NuRadioMC could be checked, for thousands of cases, but this would be outside the scope of this work. To provide concrete, verifiable comparisons, a selection of *published waveforms* generated with NuRadioMC Python packages was chosen from Figures 7 and 8 of [23]. The waveforms correspond to 10 PeV and 100 PeV electromagnetic and hadronic cascades.

The comparison involves three stages. First, waveforms and cascade profiles from NuRadioMC are digitized from Figures 7 and 8 of [23]. Second, Equations 73 and 103 are tuned to match the waveforms, and Gaussian functions are fit to the cascade profiles to obtain a -values. In each fit, the Pearson correlation coefficient (ρ) between published waveforms and Equations 73 or 103 is maximized, and the sum-squared of amplitude differences $(\Delta f)^2$ is minimized. Finally, best-fit parameters are tabulated and compared with known values quoted in [23]. Contours of correlation coefficients are shown in addition to waveform matches to illustrate the physical interpretation of theoretical parameter results.

Two remarks are important regarding the fit criteria. First, the Pearson correlation coefficient is not sensitive to differences in amplitude. The coefficient is normalized by the standard deviation of each signal, and the signals have no DC components:

$$\rho = \frac{\text{cov}(f_{\text{data}}, f_{\text{model}})}{\sigma_{\text{data}} \sigma_{\text{model}}} \quad (107)$$

Thus, the parameters that control correlation are those that scale t_r . The parameters that control $(\Delta f)^2$ are those that scale the waveform amplitude. Note that

$$(\Delta f)^2 = \sum_{i=1}^N (f_{i,\text{data}} - f_{i,\text{model}})^2 \quad (108)$$

The $(\Delta f)^2$ minimization resembles χ^2 minimization, but lacks weighting in the denominator from statistical error in the fully analytic model. No statistical error has been associated with Equations 73 and 103. The utility of minimizing $(\Delta f)^2$ is that the final difference in power between model and data is minimized.

A. Waveform Comparison: $\theta = \theta_C$

Electromagnetic case. Six different electromagnetic cascades and the corresponding Askaryan fields were drawn from Figure 7 of [23] for comparison to Equation 73. The cascades have $E_C = 10$ PeV, and $r = 1000$ meters. The units of $\vec{E}(t_r, \theta_C)$ are mV/m versus nanoseconds, so the units of $r\vec{E}$ are Volts. Plot digitization software was used to sample the waveforms and cascade profiles. After the sampling process, the effective

Nyquist frequency is 10 GHz. Let $f_C = \omega_C/(2\pi)$ and $f_{CF} = \omega_{CF}/(2\pi)$. The frequencies f_C and f_{CF} were varied from [0.05 - 3.0] GHz. The parameter E_0 was varied from [0.1 - 1.0] V GHz $^{-2}$. In a simple 3-level for-loop, the Pearson correlation coefficient ρ and sum of the squared amplitude differences $(\Delta f)^2$ were recorded for each $[\omega_C, \omega_0, E_0]$ triplet. The main results are shown in Figure 6.

Although the 3-level for-loop is an inefficient algorithm for maximizing ρ and minimizing $(\Delta f)^2$ simultaneously, it became clear that minimizing $(\Delta f)^2$ corresponded to maximizing ρ . In Figure 7, $(\Delta f)^2$ is graphed versus ρ , showing that $(\Delta f)^2$ and ρ are correlated. Thus, there was no need for independent ρ -optimization. Typical best-fit ρ -values exceed 0.97 for this set, corresponding to best-fit $(\Delta f)^2$ values of 5%. Contours of $\rho > 0.95$ for f_0 versus f_C are shown in Figure 6 (Left column). The crosses represent the best-fit location. The dashed gray line at $y = x$ corresponds to $\epsilon = 1$. Although Equation 73 contains an expansion to first order in ϵ , the motivation for the expansion is to cause the formula to resemble the derivative of the vector potential presented by ARVZ [30]. The only real restriction is that $\epsilon \neq 2$, due to the singularity. Thus, the best-fit results avoid the solid black lines ($\epsilon = 2$) in Figure 6, but find ϵ -values large enough to account for pulse asymmetry. The best-fit waveforms are shown in Figure 6 (Right column), where the gray curves correspond to NuRadioMC semi-analytic and the black curves represent Equation 73.

Table V contains the best-fit results for each parameter, along with correlation coefficients and fractional power difference. The typical fractional power difference is $\approx 5\%$, and correlation coefficients exceed $\rho = 0.97$. The exception is waveform 4, for which the digitization of the published NuRadioMC result fluctuates more than the others. This can be seen by zooming in on the gray waveform in the fourth row of Figure 6. To estimate the acceptable range for f_0 and f_C , the distance from the best-fit location to the $\rho > 0.95$ contour is computed. For f_0 , the vertical distance upwards and downwards are used respectively for the positive and negative error ranges. For f_C , the horizontal distance left and right are used respectively for the positive and negative error ranges.

The most difficult waveform features to capture when digitizing published waveforms are sharp peaks due to the line width on the published graph. Thus, best-fit frequencies for f_C do not exceed 1 GHz and are usually less than f_0 . This helps preserve the asymmetric waveform shape about $t_r = 0$, and pushes the a -values higher. Although $f_0 > f_C$ was not the default assumption in constructing the model, it is not forbidden either. Note that values of $f_C = [0.3-3]$ GHz and $\epsilon = [0.3-3]$ are expected from Figures 9 and 10 of [20]. Note also that the waveform amplitude goes as $E_0 \omega_0^2$. The error in f_0 should be assessed by varying ρ , because ω_0 alters the pulse shape in addition to the amplitude. Thus, the residual error in power, $(\Delta f)^2$, is attributed to E_0 . This is meant to be a conservative error estimate.

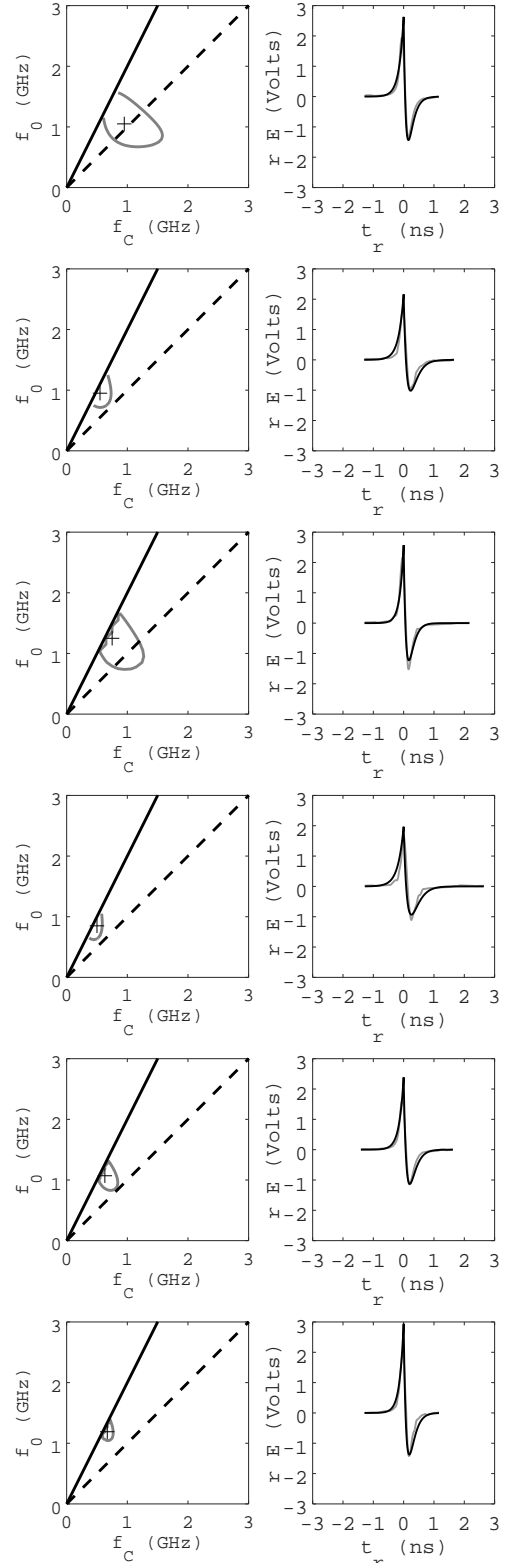


FIG. 6: **Fit results: electromagnetic case, $\theta = \theta_C$, $E_C = 10$ PeV.** The six rows (from top to bottom) correspond to NuRadioMC waveforms 1-6, 10 PeV electromagnetic cascades. (Left column) The best-fits for f_0 and f_C . Dashed line: $\epsilon = 1$. Solid line: $\epsilon = 2$. Gray contour: $\rho > 0.95$. Black cross: best-fit. (Right column) The best-fit waveforms. Gray: semi-analytic parameterizations from [23]. Black: Equation 73.

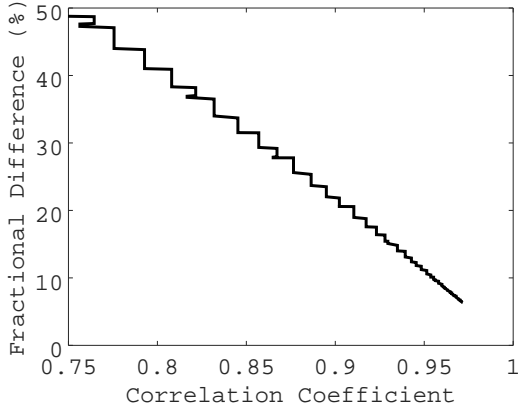


FIG. 7: The fractional difference in the sum of amplitude differences squared ($(\Delta f)^2$) versus correlation coefficient (ρ) for waveform 1 at $E_C = 10$ PeV, electromagnetic case.

#	f_0 (GHz)	f_C (GHz)	E_0 (V GHz $^{-2}$)	a (m)	l (cm)	ρ	$(\Delta f)^2$ (%)
1	$1.05^{+0.45}_{-0.3}$	$0.95^{+0.5}_{-0.3}$	0.27	$6.4^{+1.7}_{-1.0}$	$2.5^{+1.1}_{-0.7}$	0.97	5.7
2	$0.95^{+0.15}_{-0.4}$	$0.55^{+0.2}_{-0.08}$	0.89	$8.4^{+1.5}_{-0.6}$	$2.8^{+0.4}_{-1.2}$	0.97	5.7
3	$1.25^{+0.5}_{-0.2}$	$0.75^{+0.4}_{-0.1}$	0.50	$7.2^{+1.9}_{-0.5}$	$2.1^{+0.8}_{-0.3}$	0.97	5.1
4	$0.85^{+0.2}_{-0.25}$	$0.5^{+0.08}_{-0.08}$	0.92	$8.85^{+0.7}_{-0.7}$	$3.1^{+0.7}_{-0.9}$	0.92	15.9
5	$1.1^{+0.2}_{-0.15}$	$0.6^{+0.2}_{-0.1}$	0.70	$7.9^{+1.1}_{-0.5}$	$2.4^{+0.4}_{-0.3}$	0.98	4.3
6	$1.2^{+0.15}_{-0.1}$	$0.7^{+0.1}_{-0.1}$	0.94	$7.7^{+0.5}_{-0.5}$	$2.2^{+0.3}_{-0.2}$	0.97	5.4
Ave.	1.07	0.68	0.7	7.7	2.5	0.96	7
Err.	± 0.06	± 0.07	± 0.1	± 0.4	± 0.15	± 0.01	± 1.8

TABLE V: **Fit results: electromagnetic case**, $\theta = \theta_C$, $E_C = 10$ PeV. The six rows (from top to bottom) correspond to NuRadioMC waveforms 1-6, 10 PeV electromagnetic cascades. From left to right, the form-factor cutoff-frequency, coherence cutoff-frequency, energy-scaling normalization, longitudinal length parameter, the lateral width of the cascade $l = 1/(\sqrt{2\pi}\rho_0)$, the best-fit correlation coefficient, and the relative power difference between NuRadioMC semi-analytic parameterization and the fully analytic model. The parameter means and errors in the mean are quoted in the bottom two rows.

Although on-cone best-fit a -values are within a factor of 2 of the true values, Equation 103 provides precision reconstruction of a -values (see Section VI B). Though outside the scope of this work, a full-scale NuRadioMC run with thousands of waveform comparisons would reveal statistical distributions of fit parameters. Most interesting would be to constrain the region in $[f_0, f_C]$ space for which UHE- ν signals are expected for IceCube-Gen2 Radio. Thermal and man-made backgrounds that mimic UHE- ν could be rejected based on the location in $[f_0, f_C]$ space.

Hadronic case. Six different hadronic cascades and

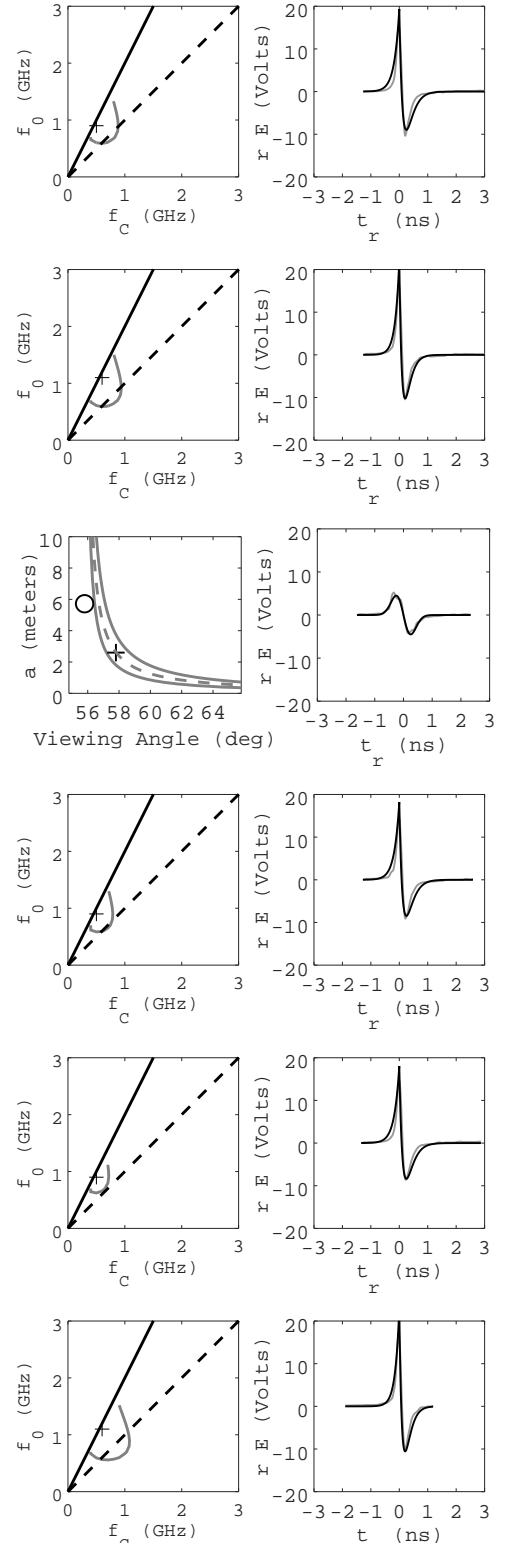


FIG. 8: **Fit results: hadronic case**, $\theta = \theta_C$, $E_C = 100$ PeV. The six rows (from top to bottom) correspond to NuRadioMC waveforms 1-6, 100 PeV hadronic cascades. (Left column) The best-fits for f_0 and f_C . Dashed line: $\epsilon = 1$. Solid line: $\epsilon = 2$. Gray contour: $\rho > 0.9$. Black cross: best-fit. (Right column) The best-fit waveforms. Gray: semi-analytic parameterizations from [23]. Black: Equation 73. Waveform 3 is treated as an off-cone ($\theta \neq \theta_C$) case. See text and Figure 9 for details.

the corresponding Askaryan fields were drawn from Figure 8 of [23] for comparison to Equation 103. The waveforms were sampled with the same procedure as the electromagnetic case. The fit procedure is also the same as the electromagnetic case, with two exceptions. First, the range for E_0 is expanded because the cascade energy is $E_C = 100$ PeV. Second, the correlation contours represent $\rho = 0.9$. In a simple 3-level for-loop, the Pearson correlation coefficient ρ and sum of the squared amplitude differences $(\Delta f)^2$ were recorded for each $[\omega_C, \omega_0, E_0]$ triplet. The main results are shown in Figure 8. Just as the results in Figure 6, minimizing $(\Delta f)^2$ corresponds to maximizing ρ .

The results shown in Figure 8 demonstrate that modeling hadronic cascades at $\theta = \theta_C$ is not fundamentally different from the electromagnetic case. The amplitudes of the best-fit analytic functions in Figure 6 are smaller by a factor of 10 due to the smaller E_C . However, the most interesting case is Waveform 3 of Figure 8, for which the corresponding 100 PeV hadronic cascade contained a sub-shower. The cascade contained a π^0 decay that led to a co-located electromagnetic cascade subject to the LPM effect. The LPM effect elongates and delays the buildup of the cascade [20] [37]. The effect on the waveform is to mimic the shape of the off-cone field equation, Equation 103. The fit procedure of Section VI B is applied (see below), and the results are $\rho = 0.98$ with $(\Delta f)^2 = 4\%$. The black cross represents the best-fit coordinates for (θ, a) , assuming the event is observed off-cone. The gray contour represents the $\rho > 0.9$ contour. The black circle represents the true values for (θ, a) . The dashed line and shape of the contour are governed by the uncertainty principle between a and $\Delta\theta$ derived in Section V A.

Table VI contains the best-fit parameters corresponding to Figure 8, along with results for ρ and $(\Delta f)^2$. The mean values for f_0 overlap with the electromagnetic case average, but the f_C results are slightly lower for the hadronic case. The result is a higher ϵ -value, indicating more asymmetry in the on-cone pulse. The exception is Waveform 3 of the hadronic case, in which the sub-shower phenomenon has smeared the pulse into a more symmetric shape that resembles Equation 103. The amplitude factors (E_0) should be a factor of 10 apart, but the ratio is closer to 14-16 due to the lower hadronic f_0 results. Since the overall amplitude goes as $E_0\omega_0^2$, lowering ω_0 (f_0) corresponds to raising E_0 . The average hadronic a -value overlaps with the average electromagnetic a -value, and both results are within a factor of 2 of the cascade-derived values of 4-5 meters. The average lateral cascade widths, l , overlap as well for both cases, and the larger l -values correspond to the larger energy. Finally, the increased asymmetry in the hadronic case leads to slightly higher $(\Delta f)^2$, but average ρ -values overlap.

#	f_0 (GHz)	f_C (GHz)	E_0 (V GHz $^{-2}$)	a (m)	l (cm)	ρ	$(\Delta f)^2$ (%)
1	$0.9_{-1.1}^{+0.3}$	$0.5_{-0.4}^{+0.01}$	12.1	$8.85_{-3.5}^{+0.03}$	$3.0_{-3.6}^{+1.0}$	0.951	9.4
2	$1.1_{-1.9}^{+0.5}$	$0.6_{-0.3}^{+0.01}$	11.1	$8.1_{-2.0}^{+0.02}$	$2.4_{-4.2}^{+1.1}$	0.96	8.5
3	4.7	--	9.0	$2.6_{-0.8}^{+1.1}$	0.6	0.98	4.0
4	$0.9_{-2.1}^{+0.3}$	$0.5_{-0.4}^{+0.01}$	11.4	$8.85_{-3.5}^{+0.02}$	$2.9_{-6.9}^{+1.0}$	0.95	10.0
5	$0.9_{-1.1}^{+0.2}$	$0.5_{-0.4}^{+0.01}$	11.3	$8.85_{-3.5}^{+0.02}$	$2.9_{-3.6}^{+0.8}$	0.94	11.8
6	$1.1_{-0.9}^{+0.5}$	$0.6_{-0.3}^{+0.01}$	11.5	$8.1_{-2.0}^{+0.02}$	$2.4_{-2.0}^{+1.2}$	0.97	6.4
Ave.	0.98	0.54	11.5	8.5	2.7	0.954	9.2
Err.	0.05	0.02	0.2	0.2	0.1	0.005	0.9

TABLE VI: **Fit results: hadronic case, $\theta = \theta_C$, $E_C = 100$ PeV.** The six rows (from top to bottom) correspond to NuRadioMC waveforms 1-6, 100 PeV hadronic cascades. From left to right, the form-factor cutoff-frequency, coherence cutoff-frequency, energy-scaling normalization, longitudinal length parameter, the lateral width of the cascade $l = 1/(\sqrt{2\pi}\rho_0)$, the best-fit correlation coefficient, and the relative power difference between NuRadioMC semi-analytic parameterization and the fully analytic model. The parameter means and errors in the mean are quoted in the bottom two rows. Waveform 3 is fit with the off-cone procedure, so there is no f_C result or error bars for f_0 and l , and the values are not included in the bottom averages (see text for details).

B. Waveform Comparison: $\theta \neq \theta_C$

Electromagnetic case. Five different electromagnetic cascades and the corresponding Askaryan fields were drawn from Figure 7 of [23] for comparison to Equation 103. In one case, only half of the $E(t_r, \theta)$ waveform is shown, so this case is not included. The waveforms were sampled in the same way as in Sec. VI A. The fit procedure is similar but not identical to Section VI A. One difference is that ω_0 only changes the waveform amplitude, along with E_0 . The pulse width $\sigma_t = \sqrt{2p}$ connects the longitudinal length a and the viewing angle with respect to the Cherenkov angle $|\Delta \cos \theta| \approx \sin \theta_C(\theta - \theta_C)$. Thus a two-stage procedure was implemented. First, θ -values and a -values were scanned from $[\theta_C + 1.5^\circ, \theta_C + 10.0^\circ]$ and $[0.1, 10]$ meters, respectively, to determine the best-fit ρ . Once the best-fit values for a and θ are determined, $(\Delta f)^2$ is minimized by varying $f_0 = \omega_0/(2\pi)$ and E_0 from $[0.3, 3.0]$ GHz and $[0.05, 5.0]$ V GHz $^{-2}$, respectively. The main results are shown in Figure 9.

In Figure 9 (Left column), the best-fit a -values and θ -values are marked with a cross. The circles represent the a -value derived from a simple Gaussian fit to the published cascade profile, and the stated θ -value of $\theta_C + 3.0^\circ$. Circles and crosses lie on the dashed lines, because an uncertainty principle connects a -values to θ -values (see Section V A). Specifically, Equation 104 may be used to show, to first-order in $\Delta\theta = \theta - \theta_C$:

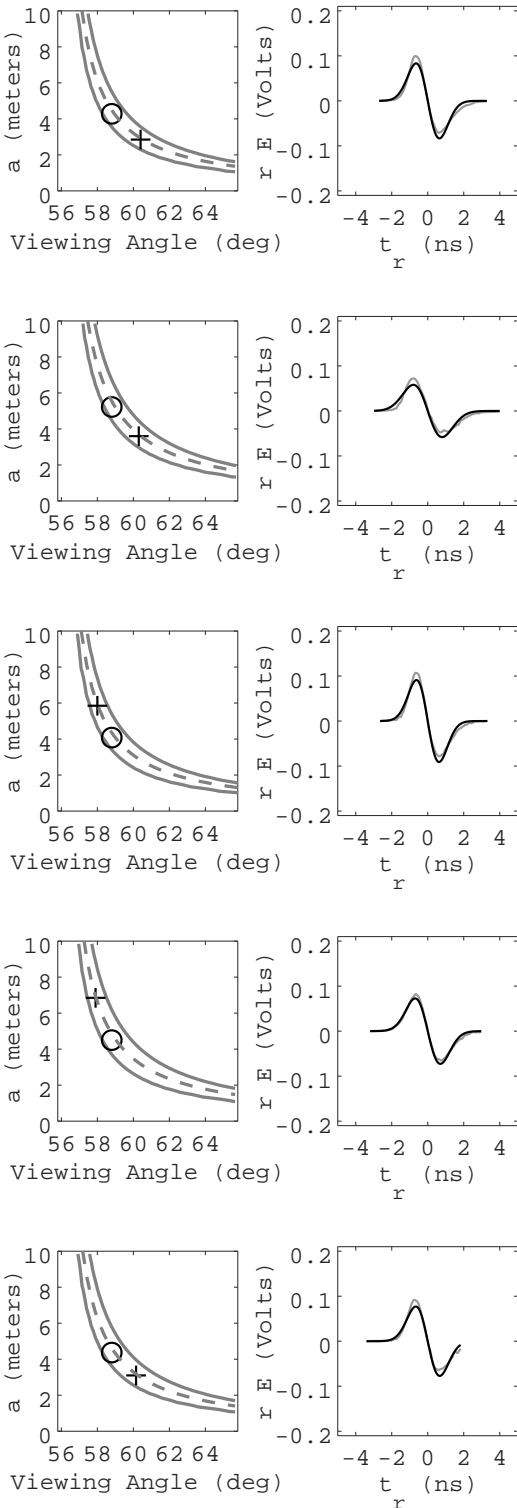


FIG. 9: **Fit results: electromagnetic case, $\theta \neq \theta_C$, $E_C = 10 \text{ PeV}$.** The five rows (from top to bottom) correspond to NuRadioMC waveforms 2-6, 10 PeV electromagnetic cascades. (Left column) Best-fit θ and a -values. Crosses: best-fits. Circles: true values. Gray contour: $\rho > 0.95$. Dashed line: a versus θ from Equation 104 (uncertainty principle). (Right column) The best-fit waveforms. Gray: semi-analytic parameterizations from [23]. Black: Equation 103.

#	θ (deg)	a (m)	f_0 (GHz)	E_0 (V GHz $^{-2}$)	l (cm)	ρ	$(\Delta f)^2$ (%)
2	$60.4^{+1.1}_{-0.9}$	$2.85^{+0.7}_{-0.55}$	2.85	1.05	$0.9^{+1.2}_{-0.9}$	0.98	3.25
3	$60.3^{+1.0}_{-0.8}$	$3.6^{+0.85}_{-0.6}$	1.0	1.15	$2.5^{+3.8}_{-3.0}$	0.975	4.9
4	$58.0^{+0.6}_{-0.4}$	$5.85^{+1.55}_{-1.2}$	4.2	1.1	$0.61^{+0.06}_{-0.05}$	0.99	2.4
5	$57.9^{+0.6}_{-0.5}$	$6.85^{+2.0}_{-1.5}$	2.9	1.1	$0.9^{+0.1}_{-0.1}$	0.99	1.2
6	$60.15^{+1.2}_{-0.9}$	$3.1^{+0.9}_{-0.6}$	1.35	1.05	$2.0^{+4.5}_{-3.2}$	0.99	2.3
Ave.	59.4	4.45	2.5	1.09	1.4	0.985	2.8
Err.	0.6	0.8	0.6	0.02	0.4	0.003	0.6

TABLE VII: **Fit results: electromagnetic case, $\theta \neq \theta_C$, $E_C = 10 \text{ PeV}$.** The five rows (from top to bottom) correspond to NuRadioMC waveforms 2-6, 10 PeV electromagnetic cascades. From left to right, the form-factor cutoff-frequency, coherence cutoff-frequency, energy-scaling normalization, longitudinal length parameter, the lateral width of the cascade $l = 1/(\sqrt{2\pi}\rho_0)$, the best-fit correlation coefficient, and the relative power difference between NuRadioMC semi-analytic parameterization and the fully analytic model. The parameter means and errors in the mean are quoted in the bottom two rows.

$$a\Delta\theta = \frac{c\sqrt{2p}}{\sin\theta_C} = \text{const} \quad (109)$$

Treating p as a constant derived from the waveform related to pulse width ($\sigma_t = \sqrt{2p}$) means that the product of a and $\Delta\theta$ is a constant. The parameters are therefore inversely proportional, and $a = \text{const}/\Delta\theta$. Further, the $\rho > 0.95$ contour is centered along the dashed lines, indicating all good fits respect the uncertainty principle. Thus, measurement of the true pulse width (beyond that introduced by RF detection components) represents a strong constraint on the event geometry. The best-fit results happen to fall above and below the true values along the dashed line, indicating no systematic bias. The best-fit waveforms are shown in Figure 9 (Right column). Typical correlation coefficients exceed $\rho = 0.97$ and typical fractional power differences are less than 5%. Table VII contains the best-fit parameters, along with ρ and $(\Delta f)^2$.

The results in Table VII demonstrate that Equation 103 is in excellent agreement with the semi-analytic parameterization. On average, the fits encounter the correct θ and a -values. Although the results for f_0 and E_0 are larger than the on-cone case, neither result is unexpected. The form-factor cutoff-frequency is a few GHz, and the amplitude E_0 is a $\mathcal{O}(1)$ unit-conversion parameter. The best-fit results for $l = 1/(\sqrt{2\pi}\rho_0)$ are pushed lower than the on-cone results due to the higher f_0 -values, but the l -values are not unexpected. Cascades with lateral spreads of a few cm should have cutoff-frequencies in the GHz range. The ρ -values are almost

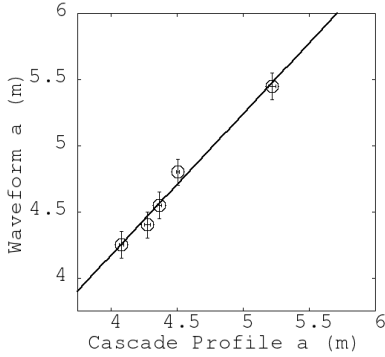


FIG. 10: The longitudinal length parameter a derived from the Equation 103 best-fit versus the a -value derived from the cascade profile. The function $f(x) = s_1x + s_2$ was fit to the data using a NLLS fit algorithm, and the parameter results are $s_1 = 1.07 \pm 0.07$ and $s_2 = -0.12 \pm 0.3$ meters.

large as possible, indicating that the *symmetric approximation* made in Section V does not incur much penalty. The fractional power differences $(\Delta f)^2$ at the few percent level, only because the fully analytic model is symmetric in amplitude.

One interesting question is whether the analytic model has potential to *reconstruct* cascade parameters from the waveform shape. What follows are two simple reconstruction exercises. For the first exercise, $\theta = \theta_C + 3.0^\circ$ is assumed fixed by another part of the analysis. For example, θ could be determined by measuring the cutoff-frequency in the Fourier domain below 1 GHz [20]. Fixing θ means a -values can be measured accurately. Scanning Equation 103 over the 10 PeV EM cascades at fixed θ yields Figure 10, in which the best-fit a -value is graphed versus the a -value obtained by fitting a Gaussian to the cascade profile. The a -errors from digitizing the cascade profiles are negligible, smaller than the marker size in Figure 10. The a -errors from waveforms are taken to be 10 cm (\pm two Δa step-sizes). A non-linear least-squares (NLLS) algorithm was applied to fit a function to the data, and a linear correlation appeared. The slope is consistent with 1.0 and y-intercept is consistent with 0.0.

The results in Figure 10 imply a reconstruction technique for $\ln(E_C)$ using the formulas found in Section III B. Consider the relationship between a and $\ln(x)$, where $x = E_C/E_{\text{crit}}$:

$$a = c_1 \sqrt{\ln(x)} \quad (110)$$

Solving for $\ln(x)$ and the error in $\ln(x)$, the result is

#	θ (deg), MC truth	θ (deg), waveform
2	58.8	58.9 ± 0.2
3	58.8	58.9 ± 0.2
4	58.8	58.9 ± 0.2
5	58.8	59.0 ± 0.2
6	58.8	58.9 ± 0.2

TABLE VIII: (Left column) Each off-cone waveform from Figure 7 of [23] is produced at $\theta = \theta_C + 3.0^\circ$, making the true θ -value 58.8 degrees in ice. (Right column) The reconstructed viewing angle from Equation 103, assuming the a -value is already known.

$$\ln(x) = (a/c_1)^2 \quad (111)$$

$$\sigma_{\ln(x)} = \sigma_a \left| \frac{d \ln(x)}{da} \right| \quad (112)$$

$$\sigma_{\ln(x)} = 2\sigma_a (a/c_1) \quad (113)$$

$$\frac{\sigma_{\ln(x)}}{\ln(x)} = 2c_1 \left(\frac{\sigma_a}{a} \right) \quad (114)$$

The final result is that the fractional error in the logarithm of energy is proportional to the fractional error in the longitudinal length parameter a .

For the second reconstruction exercise, a is assumed fixed by some other part of the analysis. For example, the energy could be reconstructed based on the slope of the Fourier spectrum [38]. Fixing a means θ can be measured accurately. Scanning Equation 103 over the 10 PeV EM cascades at fixed a yields Table VIII, in which θ derived from the waveform best-fit is compared to the MC true θ used to generate the semi-analytic waveforms [23]. The θ -error is taken to be ± 0.2 degrees (\pm two $\Delta\theta$ step-sizes). In all cases, the scan of Equation 103 yields the correct θ -value within errors. The importance of this result stems from the necessity to reconstruct the original UHE- ν direction. The ability to constrain the viewing angle is an essential component for any attempt to determine the original direction of a UHE- ν interacting in ice, along with properties like the polarization [25].

Hadronic case. Five different electromagnetic cascades and the corresponding Askaryan fields were drawn from Figure 8 of [23] for comparison to Equation 103. Only half of the sixth $E(t_r, \theta)$ waveform is shown, so this case is not included. The waveforms were sampled in the same way as in Sec. VIA. The fit procedure is the same as the electromagnetic case, except that the range for E_0 is expanded because the cascade energy is $E_C = 100$ PeV. First, θ -values and a -values were scanned from $[\theta_C + 1.5^\circ, \theta_C + 10.0^\circ]$ and $[0.1, 10]$ meters, respectively, to determine the best-fit ρ . Once the best-fit values for a and θ are determined, $(\Delta f)^2$ is minimized by varying $f_0 = \omega_0/(2\pi)$ and E_0 from $[0.3, 3.0]$ GHz and $[1.0, 20.0]$ V GHz $^{-2}$, respectively. The main results are shown in Figure 11.

As with the electromagnetic case, ρ is maximized and $(\Delta f)^2$ is minimized. Solutions with $\rho > 0.95$ are found by

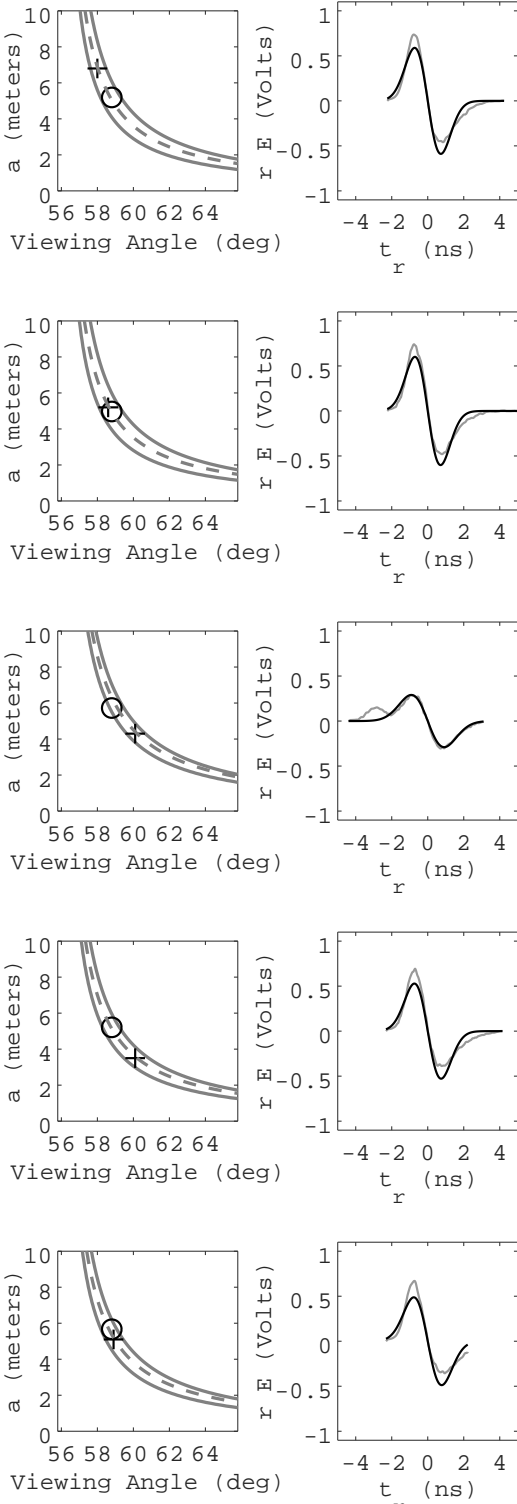


FIG. 11: **Fit results: hadronic case, $\theta \neq \theta_C$, $E_C = 100$ PeV.** The five rows (from top to bottom) correspond to NuRadioMC hadronic waveforms 1-5, 100 PeV hadronic cascades. (Left column) Best-fit θ and a -values. Crosses: best-fits. Circles: true values. Gray contour: $\rho > 0.95$. Dashed line: a versus θ from Equation 104 (uncertainty principle). (Right column) The best-fit waveforms. Gray: semi-analytic parameterizations from [23]. Black: Equation 103. Waveform 3 was generated from a cascade that included an π^0 -decay.

#	θ (deg)	a (m)	f_0 (GHz)	E_0 (V GHz $^{-2}$)	l (cm)	ρ	$(\Delta f)^2$ (%)
1	$58.0^{+0.5}_{-0.4}$	$6.8^{+1.5}_{-1.2}$	1.0	10.0	$2.6^{+0.3}_{-0.2}$	0.975	4.8
2	$58.6^{+0.6}_{-0.5}$	$5.2^{+1.2}_{-1.0}$	1.38	9.5	$1.9^{+0.5}_{-0.4}$	0.98	4.4
3	$60.1^{+0.6}_{-0.5}$	$4.3^{+0.6}_{-0.5}$	0.85	7.5	$3.0^{+4.0}_{-3.5}$	0.955	8.9
4	$60.1^{+0.75}_{-0.6}$	$3.5^{+0.6}_{-0.5}$	1.15	9.0	$2.2^{+0.4}_{-3.3}$	0.97	6.6
5	$58.9^{+0.5}_{-0.4}$	$5.1^{+0.9}_{-0.7}$	1.65	9.0	$1.55^{+0.7}_{-0.5}$	0.97	7.3
Ave.	59.1	5.0	1.2	9.0	2.25	0.970	6.4
Err.	0.4	0.5	0.15	0.4	0.25	0.004	0.8

TABLE IX: **Fit results: hadronic case, $\theta \neq \theta_C$, $E_C = 100$ PeV.** The five rows (from top to bottom) correspond to NuRadioMC waveforms 1-5, 100 PeV hadronic cascades. From left to right, the form-factor cutoff-frequency, coherence cutoff-frequency, energy-scaling normalization, longitudinal length parameter, the lateral width of the cascade $l = 1/(\sqrt{2\pi}\rho_0)$, the best-fit correlation coefficient, and the relative power difference between NuRadioMC semi-analytic parameterization and the fully analytic model. The parameter means and errors in the mean are quoted in the bottom two rows.

scanning the parameters a and θ , followed by ω_0 and E_0 . The most interesting case is Waveform 3, which is generated from a cascade with an electromagnetic sub-shower. The reason given in [23] is π^0 -decay early in the main cascade. The decay leads to an additional electromagnetic cascade subject to the LPM effect, which is delayed and elongated. This leads to a total cascade with two peaks, one of which is the largest. The fully analytic model is fitting the main peak, which generates the largest waveform contribution. The sub-shower contribution near $t_r = -3$ ns is not modeled. The pulse width is also larger than the other cases, and the amplitude is smaller. Table IX contains the best-fit parameters, along with ρ and $(\Delta f)^2$. Despite the sub-shower, $\rho > 0.95$, and $(\Delta f)^2 = 8.9\%$ for Waveform 3. Similar to the results shown in Table VII, the results in Table IX are in agreement with the true values and have $\rho > 0.95$ with power differences on the order of 6%.

VII. CONCLUSION

To advance the field of UHE- ν detection, a fully analytic Askaryan model in the time-domain has been presented, that accounts for the UHE- ν cascade energy, and lateral and longitudinal geometry. The fully analytic model was compared to published results generated with a semi-analytic parameterization used commonly in NuRadioMC, a simulation being used to design IceCube-Gen2. Pearson correlation coefficients between the fully analytic and semi-analytic parameterizations were found to be greater than 0.95, and typical fractional differences in total power were found to be 5%. What follows is a

Result	Location
$\tilde{F}(\omega, \theta)$, analytic form factor	Eq. 28, Sec. III A
$a \propto \sqrt{\ln(E_C)}$, longitudinal parameter	Eqs. 49 and 58, Sec. III B
$r\vec{E}(t_r, \theta_C)$, on-cone field ($\hat{\theta}$)	Eq. 73, Sec. IV
$\sigma_t \sigma_\nu$, on-cone uncertainty principle	Eq. 80, Sec. IV A
$r\vec{E}(t_r, \theta)$, off-cone field ($\hat{\theta}$)	Eq. 103, Sec. V
$\sigma_t \sigma_\nu$, off-cone uncertainty principle	Eq. 106, Sec. V A
On-cone EM comparison to NuRadioMC	Fig. 6, Tab. V
On-cone HAD comparison to NuRadioMC	Fig. 8, Tab. VI
Off-cone EM comparison to NuRadioMC	Fig. 9, Tab. VII
Off-cone HAD comparison to NuRadioMC	Fig. 11, Tab. IX

TABLE X: A summary of results in this work.

brief summary of new results, and a list of potential uses for a fully analytic model in UHE- ν detection.

A. Summary of New Results

The main results are summarized in Table X. Beginning with the analytic form factor, it was shown that the lateral component of the cascade ICD leads to the effect of a two-pole, low-pass filter on the radiated Askaryan field. The analytic form factor was first presented in [20], however this work has introduced the first complete study of the effect of its complex poles on the Askaryan radiation. The longitudinal factor a was introduced by Ralston and Buniy [31], who described the connection to cascade energy. In this work, a technique for cascade energy reconstruction was presented, based on constraining a -values by fitting analytic functions to observed waveforms. The connection was made for both electromagnetic cascades and hadronic cascades via common parameterizations of each cascade type.

The on-cone field equations were derived, similar to the final section of [20]. This work represents the first time the two pole frequencies f_0 and f_C and the asymmetry parameter ϵ have been used to characterize the time-domain field equations such that they match semi-analytic parameterizations with large correlation coefficients. It was shown that the on-cone field equations satisfy the uncertainty principle for Fourier transform pairs. The off-cone field equations were derived and were shown to be in excellent agreement with semi-analytic parameterizations. The potential for reconstruction exercises with the fully analytic model is especially enticing.

B. Utility of the Analytic Model

Finally, there are at least four main advantages of fully analytic models that accurately model the central Askaryan radiation peak. First, when analytic models are matched to observed data, cascade properties may

be derived directly from the waveforms. Second, in large scale simulations required for the design of IceCube-Gen2 radio, evaluating a fully analytic model technically provides a speed advantage when compared to the semi-analytic parameterizations. Third, fully analytic models, combined with RF antenna response, can be embedded in firmware to form a *matched filter* that enhances detection probability. Fourth, parameters in analytic models may be *scaled* to produce results that apply to media of different density than ice. This application is useful for understanding potential signals in the Antarctic *firn*, or the upper layer of snow and ice that is of lower density than the solid ice beneath it.

The ability to read cascade properties directly from waveforms will be a useful tool to add to the reconstruction toolkit for IceCube-Gen2 radio. Examples of current reconstruction techniques include the forward-folding method [25] and information field theory (IFT) [26]. In particular, the longitudinal length parameter a leads to a reconstruction of $\ln(E_C)$, shown in Figure 10 and Equation 114. Further, all designs for detector stations in IceCube-Gen2 radio include many distinct RF channels and one phased-array of channels. Treating each waveform like a separate trial would help increase precision on the cascade parameter reconstruction. Reconstructing the viewing angle from the pulse width, as shown in Tab. VIII, would firmly constrain the UHE- ν event geometry. Although each technique relies on knowing another parameter, even pulse width measurements without *a priori* knowledge of a or θ contain information about (θ, a) via the uncertainty principle (see gray contours of Figures 4 and 5).

Much thought has been devoted to improving the speed of NuRadioMC and other codes that rely on Askaryan emissions models. In one example, AraSim, convolution with pre-simulated cascade profiles was dropped in favor of on-the-fly convolution with the Greisen (EM) and Gaisser-Hillas (hadronic) cascade profiles [22]. While this reduced the number of steps required to produce a simulated data set, it required that a determination be made about the optimal time-window before convolution began. To help boost computation speeds in NuRadioMC, a shower library is implemented that pulls realistic cascade profiles from memory and performs the convolutions event-by-event. This strategy provides accuracy regarding randomly forming sub-showers due to the LPM effect, but it still requires a convolution for each event [23]. A fully analytic model provides fast accuracy in the energy range of 10-100 PeV without the need for a shower library.

The most intriguing usage for a fully analytic Askaryan model would be to embed the model as a *matched filter* in detector firmware. Matched filters are commonly used in radar systems that maximize detected SNR by correlating incoming data with a pre-defined function. Because the cascade properties would not be known in advance, an array of matched filters could be implemented to form a *matched filter bank*. One example of this approach was

the TARA experiment [39], which was designed to detect low-SNR cosmic ray radar echoes. This is similar to the challenge faced by IceCube-Gen2 radio: pushing the limit of low-SNR RF pulse detection in a remote setting. For example, a matched filter bank could be formed with an array of off-cone field formulas with fixed a -value and varying θ -values, which would then be convolved with the RF channel impulse response. In some cases the impulse response has been measured quite accurately [27].

Finally, a fully analytic model enhances the ability of IceCube-Gen2 radio to identify signals that originate in the firn. At the South Pole, the RF index of refraction begins around 1.35 and does not reach the solid ice value of 1.78 until 150-200 meters [28]. There are at least two signals that could originate in the firn: UHE- ν events that create Askaryan radiation, and UHE cosmic ray cascades partially inside or fully inside the firn. The altitude of the South Pole makes the latter possible. The Askaryan radiation of the firn UHE- ν events could be modeled via appropriate density-scaling of the longitudinal length a and the lateral width $1/(\sqrt{2\pi}\rho_0)$. Being lower in density, the firn would contain cascades of different size and shape relative to solid ice, which would alter the radiated E-field. The Askaryan radiation of UHE cosmic

ray cascades within the firn could be similarly modeled, with the caveat that the cosmic ray cascades would also generate geosynchrotron radiation. In the atmosphere, the geosynchrotron radiation dominates. In the firn, the UHE cosmic ray cascade would only be meters in length instead of kilometers, and the Askaryan radiation is expected to dominate.

VIII. ACKNOWLEDGEMENTS

We would like to thank our families for their support throughout the COVID-19 pandemic. We could not have completed this work without their help. We would also like to thank our colleagues for helpful discussions regarding analysis techniques. In particular, we want to thank Profs. Steve Barwick, Dave Besson, and Christian Glaser for useful discussions. Finally, we would like to thank the Whittier College Fellowships Committee, and specifically the Fletcher-Jones Fellowship Program for providing financial support for this work. This work was partially funded by the Fletcher-Jones Summer Fellowship of 2020, Whittier College Fellowships program.

[1] The IceCube Collaboration, *Science* **342**, 1242856 (2013), ISSN 0036-8075, 1311.5238.

[2] M. Ahlers, L. Anchordoqui, M. Gonzalez-Garcia, F. Halzen, and S. Sarkar, *Astroparticle Physics* **34**, 106 (2010), ISSN 0927-6505.

[3] K. Kotera, D. Allard, and A. Olinto, *Journal of Cosmology and Astroparticle Physics* **2010**, 013 (2010), ISSN 1475-7516, 1009.1382.

[4] The IceCube Collaboration, *Physical Review D* **98**, 062003 (2018), ISSN 2470-0010, 1807.01820.

[5] The ARIANNA Collaboration, *Journal of Cosmology and Astroparticle Physics* **2020**, 053 (2020), 1909.00840.

[6] The ARA Collaboration, *Physical Review D* **102**, 043021 (2020), ISSN 2470-0010, 1912.00987.

[7] M. Ackermann et al (2019), 1903.04334.

[8] M. Ackermann et al (2019), 1903.04333.

[9] J. C. Hanson et al, *Journal of Glaciology* **61**, 438 (2015), ISSN 0022-1430.

[10] J. Avva, J. Kovac, C. Miki, D. Saltzberg, and A. Vieregg, *Journal of Glaciology* (2014), 1409.5413.

[11] The ARA Collaboration, *Astroparticle Physics* **35**, 457 (2012), ISSN 0927-6505, 1105.2854.

[12] G. Askaryan, *Soviet Physics JETP* **15** (1962).

[13] E. Zas, F. Halzen, and T. Stanev, *Physical Review D* **45**, 362 (1992).

[14] The ANITA Collaboration, *Physical Review D* **99**, 122001 (2019), ISSN 2470-0010, 1902.04005.

[15] I. Kravchenko et al, *Physical Review D* **85**, 062004 (2012), ISSN 2470-0029, 1106.1164.

[16] D. Saltzberg, P. Gorham, D. Walz, C. Field, R. Iversen, A. Odian, G. Resch, P. Schoessow, and D. Williams, *Physical review letters* **86**, 2802 (2001), ISSN 0031-9007.

[17] P. Miocinovic, R. Field, P. Gorham, E. Guillian, R. Milincic, D. Saltzberg, D. Walz, and D. Williams, *Physical Review D* **74**, 043002 (2006), ISSN 2470-0029, hep-ex/0602043.

[18] P. Gorham, S. Barwick, J. Beatty, D. Besson, W. Binns, C. Chen, P. Chen, J. Clem, A. Connolly, and P. Dowkontt, *Physical review letters* **99**, 171101 (2007), hep-ex/0611008.

[19] J. Alvarez-Muñiz, A. Romero-Wolf, and E. Zas, *Physical Review D* **84**, 103003 (2011), ISSN 2470-0029, 1106.6283.

[20] J. C. Hanson and A. L. Connolly, *Astroparticle Physics* **91**, 75 (2017), ISSN 0927-6505.

[21] K. Dookayka, Ph.D. thesis, University of California, Irvine (2011).

[22] The ARA Collaboration, *Astroparticle Physics* **70**, 62 (2015), ISSN 0927-6505, URL <https://www.sciencedirect.com/science/article/pii/S0927650515000687>.

[23] C. Glaser et al, *The European Physical Journal C* **80**, 77 (2020), ISSN 1434-6044, 1906.01670.

[24] P. Glaser et al, *The European Physical Journal C* **79**, 464 (2019), ISSN 1434-6044, 1903.07023.

[25] The ARIANNA Collaboration, *Journal of Instrumentation* **15**, P09039 (2020), 2006.03027.

[26] C. Welling, P. Frank, T. A. Enßlin, and A. Nelles, arXiv (2021), 2102.00258.

[27] J. C. Hanson et al, *Astroparticle Physics* **62**, 139 (2015), ISSN 0927-6505, 1406.0820.

[28] The ARIANNA Collaboration, *Journal of Cosmology and Astroparticle Physics* **2018**, 055 (2018).

[29] The ARA Collaboration, *Astroparticle Physics* **108**, 63 (2019), ISSN 0927-6505, URL <https://www.sciencedirect.com/science/article/pii/S0927650518301154>.

- [30] J. Alvarez-Muñiz, P. M. Hansen, A. Romero-Wolf, and E. Zas, Phys. Rev. D **101**, 083005 (2020), URL <https://link.aps.org/doi/10.1103/PhysRevD.101.083005>.
- [31] R. V. Buniy and J. P. Ralston, Physical Review D **65** (2001), ISSN 2470-0029.
- [32] V. Bogorodsky, C. Bentley, and P. Gudmandsen, *Radio-glaciology* (Springer Netherlands, 1985).
- [33] S. Razzaque et al, Physical Review D **65**, 103002 (2002), ISSN 2470-0029, astro-ph/0112505.
- [34] M. Abramowitz and I. A. Stegun, *Handbook of Mathematical Functions with Formulas, Graphs, and Mathematical Tables* (Dover, New York City, 1964).
- [35] DLMF, *NIST Digital Library of Mathematical Functions*, <http://dlmf.nist.gov/>, Release 1.1.1 of 2021-03-15, f. W. J. Olver, A. B. Olde Daalhuis, D. W. Lozier, B. I. Schneider, R. F. Boisvert, C. W. Clark, B. R. Miller, B. V. Saunders, H. S. Cohl, and M. A. McClain, eds., URL <http://dlmf.nist.gov/>.
- [36] T. T. García, Monthly Notices of the Royal Astronomical Society **369**, 2025 (2006), ISSN 0035-8711.
- [37] L. Gerhardt and S. R. Klein, Phys. Rev. D **82**, 074017 (2010), URL <https://link.aps.org/doi/10.1103/PhysRevD.82.074017>.
- [38] S. Barwick, D. Besson, A. Burgman, E. Chiem, A. Hallgren, J. Hanson, S. Klein, S. Kleinfelder, A. Nelles, C. Persichilli, et al., Astroparticle Physics **90**, 50 (2017), ISSN 0927-6505, 1612.04473.
- [39] The Telescope Array Collaboration, Astroparticle Physics **87**, 1 (2017), ISSN 0927-6505, URL <https://www.sciencedirect.com/science/article/pii/S0927650516301682>.